University of Reading

# *Is the surface salinity difference between the Atlantic and Indo–Pacific a signature of the Atlantic Meridional Overturning Circulation?*

Article

Accepted Version

Nilsson, J., Ferreira, D. ORCID: https://orcid.org/0000-0003-3243-9774, Schneider, T. and Wills, R. C. J. (2020) Is the surface salinity difference between the Atlantic and Indo–Pacific a signature of the Atlantic Meridional Overturning Circulation? Journal of Physical Oceanography. ISSN 0022-3670 doi: https://doi.org/10.1175/JPO-D-20-0126.1 Available at http://centaur.reading.ac.uk/95049/



To link to this article DOI: http://dx.doi.org/10.1175/JPO-D-20-0126.1

Publisher: American Meteorological Society

# Is the surface salinity difference between the Atlantic and Indo–Pacific a signature of the Atlantic Meridional Overturning Circulation?

Johan Nilsson*

*Department of Meteorology, Stockholm University, Stockholm, Sweden*

David Ferreira

*Department of Meteorology, University of Reading, Reading, United Kingdom*

Tapio Schneider

*California Institute of Technology, Pasadena, California*

Robert C. J. Wills

*Department of Atmospheric Sciences, University of Washington, Seattle, Washington*

**Corresponding author*: nilsson@misu.su.se

ABSTRACT

The high Atlantic surface salinity has sometimes been interpreted as a signature of the Atlantic Meridional Overturning Circulation and an associated salt advection feedback. Here, the role of oceanic and atmospheric processes for creating the surface salinity difference between the Atlantic and Indo–Pacific is examined using observations and a conceptual model. In each basin, zonally averaged data are represented in diagrams relating net evaporation ($\tilde{E}$) and surface salinity ($S$). The data-pair curves in the $\tilde{E}$–$S$ plane share common features in both basins. However, the slopes of the curves are generally smaller in the Atlantic than in the Indo–Pacific, indicating a weaker sensitivity of the Atlantic surface salinity to net evaporation variations. To interpret these observations, a conceptual advective-diffusive model of the upper-ocean salinity is constructed. Notably, the $\tilde{E}$–$S$ relations can be qualitatively reproduced with only meridional diffusive salt transport. In this limit, the inter-basin difference in salinity is caused by the spatial structure of net evaporation, which in the Indo–Pacific oceans contains lower meridional wavenumbers that are weakly damped by the diffusive transport. The observed Atlantic $\tilde{E}$–$S$ relationship at the surface reveals no clear influence of northward advection associated with the meridional overturning circulation; however a signature of northward advection emerges in the relationship when the salinity is vertically averaged over the upper kilometer. The results indicate that the zonal-mean near-surface salinity is shaped primarily by the spatial pattern of net evaporation and the diffusive meridional salt transport due to wind-driven gyres and mesoscale ocean eddies, rather than by salt advection within the meridional overturning circulation.

## Abstract

The high Atlantic surface salinity has sometimes been interpreted as a signature of the Atlantic Meridional Overturning Circulation and an associated salt advection feedback. Here, the role of oceanic and atmospheric processes for creating the surface salinity difference between the Atlantic and Indo–Pacific is examined using observations and a conceptual model. In each basin, zonally averaged data are represented in diagrams relating net evaporation ($\tilde{E}$) and surface salinity ($S$). The data-pair curves in the $\tilde{E}$–$S$ plane share common features in both basins. However, the slopes of the curves are generally smaller in the Atlantic than in the Indo–Pacific, indicating a weaker sensitivity of the Atlantic surface salinity to net evaporation variations. To interpret these observations, a conceptual advective-diffusive model of the upper-ocean salinity is constructed. Notably, the $\tilde{E}$–$S$ relations can be qualitatively reproduced with only meridional diffusive salt transport. In this limit, the inter-basin difference in salinity is caused by the spatial structure of net evaporation, which in the Indo–Pacific oceans contains lower meridional wavenumbers that are weakly damped by the diffusive transport. The observed Atlantic $\tilde{E}$–$S$ relationship at the surface reveals no clear influence of northward advection associated with the meridional overturning circulation; however a signature of northward advection emerges in the relationship when the salinity is vertically averaged over the upper kilometer. The results indicate that the zonal-mean near-surface salinity is shaped primarily by the spatial pattern of net evaporation and the diffusive meridional salt transport due to wind-driven gyres and mesoscale ocean eddies, rather than by salt advection within the meridional overturning circulation.


## 1. Introduction

The global meridional overturning circulation (MOC) exchanges water between the surface and deep ocean and between the major ocean basins (Marshall and Speer 2012; Talley 2013; Cessi 2019).

The MOC transports heat, freshwater and biogeochemical tracers, thereby influencing climate and the cycling of carbon and nutrients in the ocean (Talley 2003; Sarmiento and Toggweiler 1984; Galbraith and de Lavergne 2019). The Atlantic MOC (AMOC) is associated with a northward transport of upper ocean water toward northern sites of deep sinking, and a southward transport of deep water (Wunsch and Heimbach 2013; Cessi 2019). A striking inter-basin asymmetry of the MOC is the absence of a strong Pacific MOC and of deep sinking in the North Pacific.

A fundamental and yet unresolved question is why there is an AMOC but no Pacific MOC (PMOC) in the present climate (Huisman et al. 2012; Ferreira et al. 2018; Weijer et al. 2019). It is well established that it is the contrast in surface salinity between the Pacific and the Atlantic that prevents deep sinking in the North Pacific (Weyl 1968; Warren 1983): In the North Pacific, surface water is fresher and lighter than the deep water, which is close to the mean deep-water salinity of the world ocean. However, the salinity contrast in itself provides no satisfying process-based explanation, and there are diverging ideas of why this contrast arises. Several hypotheses have been proposed to explain the asymmetry in circulation and salinity between the two basin. These hypotheses fall into two main categories (see Ferreira et al. 2018, for a review):

H1: The salinity contrast is set by differences in net evaporation over the basins. Here, the Atlantic–Pacific difference in the surface freshwater balance is primarily viewed to be created by zonal asymmetries of the atmospheric circulation and the drainage basins (Weyl 1968; Emile-Geay et al. 2003; Ferreira et al. 2010; Wills and Schneider 2015). To the extent that the atmospheric circulation is not modified by changes in the MOC, a single equilibrium state of the MOC is expected.

H2: The salinity contrast is set by differences in oceanic salt transports. Asymmetries in basin geometry and wind forcing as well as the oceanic salt-advection feedback contribute to elevate the Atlantic salinity (Reid 1961; Stommel 1961; Warren 1983; Nilsson et al. 2013; Jones and Cessi 2017; Weijer et al. 2019). The MOC may have multiple equilibrium states.

The asymmetry in salinity likely results from a combination of these atmospheric and oceanic processes, but their relative importance remains uncertain. Several asymmetries in mountain range distributions and ocean basin geometry have been identified that act to increase Atlantic surface salinities relative to the Pacific, either by affecting the net evaporation or the oceanic salt transports (Seager et al. 2002; Maffre et al. 2018; Reid 1961; Nilsson et al. 2013; Jones and Cessi 2017). However, progress has been limited in quantifying the numerous proposed processes and in determining their relative importance. A quantitative understanding of the geographical and climatic factors that determine the sinking locations in the world ocean is of fundamental significance. First, when developing present-day climate models, or even upgrading existing ones, some models can yield a PMOC rather than an AMOC, or a strongly reduced AMOC compensated by increased Southern Ocean sinking (see Mecking et al. 2016; Ferreira et al. 2018, and references therein). This may indicate that the geographical features assumed to favour Atlantic sinking are rather weak; or that their impacts are inadequately represented in some climate models. The AMOC "problem" is usually addressed by tuning of model parameters and drainage pathways until a realistic AMOC is obtained; an approach that may yield a model AMOC with incorrect stability features and sensitivity to global warming (Stouffer et al. 2006; Cimatoribus et al. 2012; Weijer et al. 2019; Cael and Jansen 2020). Second, the locations of the deep sinking and associated MOC pathways in past epochs of the Earth can have a strong influence on carbon cycling and climate (DeConto and Pollard 2003; Ferrari et al. 2014; Galbraith and de Lavergne 2019). Thus, knowledge of which aspects of the basin geometry and climatic conditions control the MOC is crucial for understanding the ocean's role in past as well as future climate transitions.

Motivated by these broader questions concerning the ocean salinity distribution and the MOC, we here explore and develop a diagnostic concept introduced by Ferreira et al. (2018): to analyse zonally-averaged observations in evaporation–salinity diagrams. This representation encapsulates the forcing (net evaporation) and the response (surface salinity). Specifically, we extend the work of Ferreira et al. (2018) to analyse zonally-averaged observations with higher latitudinal resolution in evaporation–salinity diagrams and to interpret the results using a conceptual advective-diffusive model. We begin by briefly examining observations of zonal-mean net evaporation and surface salinity. Next, we introduce and analyze the conceptual model, and then return to the observations and discuss what they can tell us about the relative importance of atmospheric and oceanic processes in setting the present-day Atlantic–Pacific salinity asymmetry.

## 2. The observed relationship between zonal-mean net evaporation and surface salinity

Here, we analyze net evaporation data from ERA-Interim reanalysis for the period 1979-2012 (Dee et al. 2011), with treatment of continental runoff as described in Wills and Schneider (2015), and climatological surface salinity from the World Ocean Atlas 2013 (Zweng et al. 2013). The climatological salinity is based on observations taken between 1955 and 2012, but by construction it is more influenced by the data-rich later part of the period. We have also calculated and analyzed a time-mean salinity based on the individual decadal data from 1975 to 2012 in the World Ocean Atlas 2013. For the time-mean relationship between zonal-mean net evaporation and surface salinity, which is our focus, the difference in using the 1975-2012 mean and the climatological salinity is small enough that we for simplicity have chosen to use the standard climatological salinity in the World Ocean Atlas 2013.

The surface salinity variations are forced by freshwater fluxes at the sea surface, acting to change the salinity at a rate proportional to the net evaporation. As there are essentially no feedbacks between the surface salinity and net evaporation (Stommel 1961; Haney 1971), the steady-state surface salinity distribution is controlled by a balance between the surface freshwater fluxes and the rate at which advective and diffusive processes redistribute salinity[1] in the ocean (Schmitt 2008; Hieronymus et al. 2014; Zika et al. 2015; Ponte and Vinogradova 2016). As a result, there is a general correlation between net evaporation and surface salinity, which is apparent in the zonally-averaged observations shown in Fig. 1. Here, the zonally-averaged net evaporation ($\tilde{E}$) includes continental runoff

$$\tilde{E} \stackrel{\text{def}}{=} E - P - R, \tag{1}$$

and $E$, $P$ and $R$ are the zonally-averaged evaporation, precipitation, and runoff, respectively. In all ocean basins, high surface salinities are encountered in the dry subtropical regions, and lower salinities are encountered in the wet tropical and high-latitude regions. The North Atlantic is generally more evaporative than the North Indo–Pacific, but discharge from the Amazon River contributes to a strong zonal-mean net precipitation (i.e. $\tilde{E} < 0$) in the equatorial Atlantic (Craig et al. 2017). The salinity fields appear slightly smoother than the net evaporation fields, indicating that scale-selective damping suppresses the smaller scales of the net evaporative forcing.

Figure 1 also reveals some deviations from a simple one-to-one relation between $\tilde{E}$ and $S$, particularly when the Atlantic and Indo–Pacific are compared. These deviations can be illuminated by representing the zonally-averaged observations in a diagram spanned by net evaporation ($x$ axis) and surface salinity ($y$ axis). The $\tilde{E}$–$S$ diagrams combine the forcing (net evaporation) with the response (surface salinity) and encapsulate information on the efficiency of oceanic processes in damping surface salinity variations. Figure 2 shows $\tilde{E}$–$S$ diagrams for the Atlantic and Indo–

[1]In a steady state, it is freshwater and not salt that is transported; but the freshwater transport multiplied by a mean ocean salinity can by viewed as a virtual salt transport (Craig et al. 2017).

Pacific, where the data have been zonally-averaged in 5° wide latitude bands[2]. The $\tilde{E}$ and $S$ data pairs from different latitude bands do not fall on a straight lines. Instead, the data trace out curves in the $\tilde{E}$–$S$ plane with slopes that vary latitudinally and yield multivalued relations between surface salinity and net evaporation. There are a few noteworthy general features of the $\tilde{E}$–$S$ curves:

1. Their slopes are smaller in the tropics than in the extratropics.
2. The curves tend to turn and loop near the subtropical salinity maxima: progressing poleward the curves turn anticlockwise.
3. In the Indo–Pacific, the $\tilde{E}$–$S$ relation is more equatorially asymmetric and indicates a higher salinity sensitivity to variations in net evaporation than in the Atlantic. (Progressing away from the black markers in Fig. 2, the curves are approximately parallel in the Atlantic, but not in the Indo–Pacific, where the equatorial asymmetry is larger.)

We will try to explain these features using the conceptual model described below. The bending of the $\tilde{E}$–$S$ curves in the subtropics reflect that the salinity maxima are encountered slightly poleward of the maxima in net evaporation (Gordon et al. 2015; Ponte and Vinogradova 2016). This poleward shift can also be seen by comparing the latitudinal distribution of the zonal-mean net evaporation and salinity in Fig. 1, but the shift is more conspicuous in the $\tilde{E}$–$S$ diagram.

The local slopes of the $\tilde{E}$–$S$ curves between nearby latitude points measure salinity sensitivity to variations in net evaporation. However, the local slopes are sensitive to the latitudinal averaging window and to whether centered or one-sided differences are used to calculate them; they can be negative, and generally there will be a few latitude points that will have very large positive or

[2]We exclude marginal seas in the zonal-mean surface salinity but include them in the zonally-averaged $\tilde{E}$, taken over the associated drainage basins. This affects only the Atlantic salinities, where low surface salinities in the Black and Baltic Seas distort the Atlantic zonal-mean salinity profile if included in the Atlantic zonal mean (Fig. 1b). Our rationale is that these low salinities reflect constricted exchange of the marginal seas rather than features of the open Atlantic Ocean circulation. This choice does not qualitatively affect the Atlantic $\tilde{E}$–$S$ relationship.

negative slopes. A more robust way to measure the sensitivity is obtained by following Ferreira et al. (2018) to calculate an overall salinity sensitivity by fitting, in a least-squares sense, a straight line to the data points

$$S(\tilde{E}) = S_T + k\tilde{E}, \tag{2}$$

where $S_T$ is the fitted ”target” salinity at $\tilde{E} = 0$ and $k$ is the slope. A least squares fit of the data points between 40°S and 65°N give a slope in the Atlantic (Indo–Pacific) that corresponds to a salinity change of 0.7 (1.3) psu per m year$^{-1}$. We have calculated the regression slopes in $\tilde{E}$–$S$ diagrams using latitudinal binning of the data ranging from 5 to 20 degrees (not shown). The slopes increase slightly with the binning width, but the ratio between the Atlantic and Indo–Pacific slopes is essentially constant up to a binning width of 15 degrees (see below). The calculated regression slopes indicate that the surface salinity sensitivity to net evaporation variations is nearly twice as large in the Indo–Pacific Basin as in the Atlantic Basin.

In a surface ocean layer of depth $h$, a salinity damping timescale $\tau$ can be estimated as (Ferreira et al. 2018)

$$\tau = \frac{\Delta S}{\Delta \tilde{E}} \frac{h}{S_0}, \tag{3}$$

where $\Delta S$ and $\Delta \tilde{E}$ are the ranges in salinity and net evaporation, respectively, and $S_0 = 35$ psu a constant reference salinity. Using the regression slope defined in Eq. (2), one can estimate the ratio $\Delta S/\Delta \tilde{E} \approx k$, and hence obtain the damping timescale as $\tau \approx kh/S_0$. For example, if we take a surface layer of 100 m thickness, the regression slope in Fig. 2 gives a damping timescale of 2 (4) years in the Atlantic (Indo–Pacific). Estimates of salinity damping timescales based on observations and modelling give timescales ranging from a few years in the ocean mixed layer (Hall and Manabe 1997) to several decades in interior ocean (Williams et al. 2006; Zika et al. 2015; Ferreira et al. 2018).

Regional details in Fig. 2 can be removed by calculating more coarse-grained $\tilde{E}$–$S$ diagrams, based on area-averages in wider latitude bands. This is in effect a spatial low-pass filtering that reduces the range in salinity and net evaporation. Main features of the $\tilde{E}$–$S$ curves in Fig. 2 can still be identified in diagrams based on latitude bands of 10 to 15 degrees width (not shown). Binning in uniform latitude bands wider than about 15 degrees no longer adequately samples the structure of the data, and the results become dependent on the binning width. However, an illuminating large-scale view is obtained by selecting ocean-circulation regimes as in Ferreira et al. (2018): southern/northern subtropical regions (40°S–0°/0°–40°N) and northern subpolar regions (40°N–65°N); where the subtropics roughly encompass the wet near-equatorial and dry subtropical regions that host the oceanic subtropical cells and gyres. Figure 3 shows the corresponding $\tilde{E}$–$S$ diagram. As discussed by Ferreira et al. (2018), the data within the Atlantic and Indo–Pacific basins fall approximately on two straight lines, describing generally higher Atlantic salinities and a stronger sensitivity (steeper slope) in the Indo–Pacific.

This preliminary analysis of the $\tilde{E}$–$S$ diagrams brings up two questions. First, can the zonal-mean observations reveal additional information on whether it is primarily differences in net evaporation or ocean processes that cause the apparent higher sensitivity in the Indo–Pacific Ocean: Is the basin difference in salinity explained chiefly by hypothesis H1 or H2? Second, can the shapes of the $\tilde{E}$–$S$ curves reveal information on which oceanic processes control the damping of the surface salinity? Specifically, can a signature of the Meridional Overturning Circulation be detected in the $\tilde{E}$–$S$ relations? To examine these questions, we will consider a simple advective–diffusive model of the zonal-mean upper ocean salinity. We will return to the interpretation of the observations after examining the conceptual model.

## 3. Relationship between net evaporation and surface salinity: a conceptual advective-diffusive model

The zonal-mean surface salinity is affected by meridional advection and diffusion as well as vertical salt fluxes (Ponte and Vinogradova 2016). The zonal-mean near-surface meridional flow is dominated by wind-driven Ekman transports and is generally directed poleward in the tropics and equatorward in the extratropics (Schott et al. 2013; Gordon et al. 2015). Hence, the near-surface zonal-mean flow has meridional structure, which implies vertical motion. The wind-driven gyres have only a small impact on the zonal-mean meridional flow. However, zonal shears of the gyres and vertical shears of shallow subtropical cells (McCreary and Lu 1994; Nilsson and Körnich 2008; Schott et al. 2013) as well as their seasonal and inter-annual variations, increase the effective meridional diffusivity on the zonally-averaged salinity in the near-surface ocean (Rhines and Young 1983; Young and Jones 1991; Wang et al. 1995; Rose and Marshall 2009; Jones and Cessi 2018).

For simplicity, we neglect the meridional structure of the near-surface flow and examine how constant northward advection and diffusive transport affect the zonal-mean sea-surface salinity and its relation to the net evaporation in a conceptual model. Specifically, we consider a model of the zonal-mean salinity in an upper-ocean layer with constant depth $h$ and zonal width $B$ (Fig. 4). In the upper layer, the salinity ($S$), meridional velocity ($v$), and meridional diffusivity ($\kappa$) are assumed to depend only on the meridional coordinate $y$. An entrainment velocity $w_e$ is used to model vertical diffusive salt fluxes between the surface layer and the interior ocean, which has a constant salinity $S_d$. The advective velocity represents a meridional overturning circulation with a constant northward volume transport ($\psi$) in the upper layer given by

$$\psi = vBh. \tag{4}$$

The upper-layer volume flow is assumed to return southward in an interior layer, which is not represented in the model. The domain is an ocean basin limited by vertical walls at its the southern and northern ends. With these assumptions, the upper-layer steady-state salinity equation is given by

$$\psi \frac{dS}{dy} - \frac{d}{dy}\left(Bh\kappa \frac{dS}{dy}\right) + Bw_e(S - S_d) = B\tilde{E}S_0. \tag{5}$$

Here, the term $B\tilde{E}S_0$ is the surface forcing, and the left-hand side represents oceanic processes that damp salinity variations. The vertical mixing term $Bw_e(S - S_d)$ by itself gives a linear relation between $S$ and $\tilde{E}$. We begin by neglecting vertical mixing and focus on the advective and diffusive terms.

In the model calculations, we consider $\tilde{E}$ fields that integrate to zero over the model domain. For $\psi = 0$, this allows solutions to Eq. (5) to satisfy a zero diffusive flux condition (i.e., $dS/dy = 0$) at the northern and southern basin boundaries. For non-zero advection, the diffusive flux cannot generally be zero at both the boundaries. This is a consequence of non-zero $v$; if the salinity is not the same at both boundaries, then there will be advective convergence or divergence that must be balanced by diffusive boundary fluxes. A more complex model with an active layer is needed to ensure salt conservation. As we will show, however, the simple one-layer model yields advective-diffusive solutions that are physically relevant if they satisfy a zero diffusive flux condition at the northern boundary (say $y = y_n$)

$$\left(\frac{dS}{dy}\right)_{y=y_n} = 0. \tag{6}$$

The impact of this boundary condition decays exponentially from the northern boundary, which yields advective-diffusive solutions that reproduce aspects of the observations; further physical considerations and technical details related to the boundary conditions are discussed in the appendix.

When $B$ and $\kappa$ are constant and $w_e = 0$, the salinity equation simplifies to the advection–diffusion equation

$$v\frac{dS}{dy} = \kappa\frac{d^2S}{dy^2} + S_0\tilde{E}/h. \qquad (7)$$

Below, we will consider some simple and illustrative solutions to Eq. (7).

### *a. A simple harmonic net evaporation field*

First, we consider an ”ocean” extending from $y = -L$ to $y = L$ and examine solutions to Eq. (7) forced by an equatorially-symmetric evaporation field described by a single cosine function

$$\tilde{E}(y) = \hat{E}\cos(2\pi y/L), \qquad (8)$$

where $\hat{E} < 0$ is the amplitude (Fig. 4). This idealized field has wet tropical and polar latitude bands with dry subtropical regions in between. To obtain a solution for the salinity field, we make the ansatz

$$S(y) = a\cos(ly) + b\sin(ly), \qquad (9)$$

where $l = 2\pi/L$ is the meridional wavenumber. By inserting this expression into Eq. (7) and using the linear independence of the cosine and sine functions, we can determine $a$ and $b$. The result can be written as

$$S(y) = \hat{S}\cos(ly - \phi). \qquad (10)$$

Here, we have introduced a salinity amplitude $\hat{S}$ and a phase $\phi$

$$\hat{S} \stackrel{\text{def}}{=} \frac{S_0\hat{E}\tau_{ad}}{h}, \qquad \tan(\phi) \stackrel{\text{def}}{=} \frac{v}{\kappa l}, \qquad (11)$$

where the timescale

$$\tau_{ad} \stackrel{\text{def}}{=} [(\kappa l^2)^2 + (vl)^2]^{-1/2}, \qquad (12)$$

is an effective damping timescale due to horizontal advection and diffusion. The Peclet number

$$\mathrm{Pe} \stackrel{\mathrm{def}}{=} vL/\kappa, \tag{13}$$

measuring the relative importance of advection and diffusion, is related to the phase $\phi$ as $\mathrm{Pe} = 2\pi\tan(\phi)$. In the model calculations, we will only consider northward advection ($v > 0$), implying that $\mathrm{Pe} > 0$ as defined in Eq. (13). However, it is common practice to only use positive Peclet numbers, and we will follow this when discussing advection due to zonal-mean surface Ekman transports that can be northward as well as southward.

Using Eqs. (8) and(10), the evaporation–salinity relation can be written as

$$[\tilde{E}, S] = [\hat{E}\cos(ly), \hat{S}\cos(ly - \phi)], \tag{14}$$

where $ly$ ranges from $-2\pi$ to $2\pi$. This equation describes a family of elliptical curves[3] in the $\tilde{E}$–$S$ plane, which have two limiting cases:

1. A diffusive limit ($v = 0$), where $\phi = 0$ and the ellipse reduces to a straight-line segment. For fixed values of $v$ and $\kappa$, this limit is approached as the wavenumber $l$ becomes large.

2. An advective limit ($\kappa = 0$) where $\phi = \pi/2$ and the salinity is shifted 90 degrees downstream relative to the net evaporation. Here, Eq. (14) describes a closed ellipse. For fixed values of $v$ and $\kappa$, this limit is approached as the wavenumber $l$ becomes small compared to $v/\kappa$.

Figure 5a shows evaporation–salinity relations Eq. (14) for phases given by $\phi = 0$ ($\mathrm{Pe} = 0$) and $\phi = \pi/7$ ($\mathrm{Pe} \approx 3$). For non-zero advection, the relation between $\tilde{E}$ and $S$ is multivalued: For each value of $\tilde{E}$, there is one higher and one lower value of $S$, which in physical space, are located upstream and downstream of the extrema in $\tilde{E}$, respectively.

[3]If $\hat{E}$ and $\hat{S}$ are normalized to unity, the major axis of the ellipse is tilted 45 degrees relative to the $x$-axis and the ratio between the minor and major axes is $\sin(\phi)$.

By using Eqs. (11) and (12), we find that, in the diffusive limit, the slope of the $\tilde{E}$–$S$ curve is

$$\left(\frac{dS}{d\tilde{E}}\right)_y = \frac{S_0}{h\kappa l^2}. \tag{15}$$

Hence, the slope is controlled jointly by features characterizing the oceanic diffusive transport ($h\kappa$) and the meridional wavenumber of net evaporation field ($l$). Note that the slope is proportional to the oceanic damping timescale, which in the diffusive limit is $(\kappa l^2)^{-1}$. This is in correspondence with Eq. (3) that also relates damping timescale and slope in $\tilde{E}$–$S$ diagrams.

For non-zero values of $v$, the solution described by Eq. (10) does not satisfy the boundary condition of zero diffusive flux at the northern basin edge (Eq. 6). To meet this condition, we add a homogenous solution of Eq. (7)

$$S_H(y) = A + B\exp[\mathrm{Pe}(y/L)], \tag{16}$$

where $A$ and $B$ are constants. The appendix outlines how solutions satisfying the boundary condition Eq. (6) can be obtained. In the tropics, a zonal-mean velocity based on the poleward flow in the wind-driven surface Ekman layer yields $v \sim 0.01$ m s$^{-1}$ (a typical Ekman transport distributed over a 50 m surface layer) and eddy diffusivity estimates suggest that $\kappa \sim 5 \cdot 10^3$ m$^2$ s$^{-1}$ (Abernathey and Marshall 2013). Taking a length scale characterizing the distance between the subtropical extrema in net evaporation ($L \sim 2 \cdot 10^6$ m) yields Pe $\sim 4$, suggesting that meridional Ekman advection should be important for the surface salinity budget. As we will discuss further below, however, wind-driven gyres contribute to meridional diffusion of the zonal-mean salinity. This increases the effective meridional diffusivity and decreases the Peclet number.

Figure 5b shows the evaporation–salinity relation for $\phi = \pi/7$ (corresponding to Pe $\approx 3$) where the homogeneous salinity solution Eq. (16) has been added to satisfy the northern boundary condition of zero diffusive flux (Eq. 6). This increases the strength of the advection relative to diffusion near the northern boundary and elevates the salinity. However, there is no salt-advection feedback

(Stommel 1961) as the velocity is prescribed and independent of the salinity in the model. The homogenous solution increases the salinity going northward, and the resulting $\tilde{E}$–$S$ curve in Fig. 5b is no longer a closed ellipse, but rather a spiral: progressing from south to north across the wet and dry zones the salinity increases gradually.

The simple cosine evaporation field illustrates how advection can shift the salinity extrema relative to the net evaporation extrema, causing a multi-valued $\tilde{E}$–$S$ relation. However, these advective $\tilde{E}$–$S$ relation are rather different from the observed ones (Fig. 2). We will now show that the main differences are related to the more complex spatial structure of the real net evaporation fields.

### *b. Solutions for equatorially-symmetric net evaporation fields*

There are two equatorially-symmetric features of the real net evaporation distribution (Fig. 1a) that differ from the simple single-wavenumber cosine field (Eq. 8, Fig. 4). First, the peak in net evaporation is located closer to the equator than to the pole. Second, the amplitude of the wet equatorial extremum is larger than the amplitudes of the dry subtropical and wet subpolar extrema. Primarily, this reflects the narrow ascending regions of the Hadley circulation that confine the net precipitation in the Inter Tropical Convergence Zones. These features cannot be represented by a single wavenumber cosine function and additional higher wavenumber must be included in a Fourier series expansion of $\tilde{E}(y)$. Due to the scale-selective advective-diffusive salinity damping in the conceptual model, inclusion of higher wavenumber in the freshwater forcing yields a muted salinity response, which alters the $\tilde{E}$–$S$ relation. It should be emphasised, however, that for a given $\tilde{E}$ field, the shape of the salinity solutions to Eq. (7) still depends only on the Peclet number Pe and the boundary conditions.

Here, we use an $\tilde{E}$ field based on the equatorially-symmetric component of the net evaporation field in the Atlantic (Fig. 1a), with a constant added to make the area-integrated net evaporation zero in the model basin. Figure 6a shows this $\tilde{E}$ field and corresponding salinity solutions for two Peclect numbers. In effect, the scale selective damping causes the salinity fields to be spatially low-passed filtered versions of the $\tilde{E}$ field. In the diffusive limit (Pe = 0), the salinity field is equatorially symmetric. Non-zero northward advection (Pe = 2, where the boundary condition Eq. 6 is used) breaks the symmetry by increasing the salinity in the northern hemisphere relative to the southern hemisphere.

Figure 7 shows the $\tilde{E}$–$S$ relations for the "Atlantic-like" $\tilde{E}$ field, which is constructed to be symmetric about the equator. In contrast to the single wavenumber case, the diffusive limit does not yield a straight line in the $\tilde{E}$–$S$ diagram (Fig. 7a). There are now two branches: one tropical with a weaker slope and one extratropical with a steeper slope, which reflects the smaller meridional length scale (or equivalently stronger curvature) of $\tilde{E}(y)$ in the tropics[4]. Notably, the scale-selective diffusive damping yields higher salinities at the equator than in the subpolar regions, despite that the net precipitation is higher near the equator. In addition, the $\tilde{E}$–$S$ curve makes a loop and crosses itself near the subtropical salinity maximum. Accordingly, the spatial features of the net evaporation can shift the extrema in $S$ relative to the extrema in $\tilde{E}$ even in the limit of diffusive transport.

The underlying physics is straightforward and can be illustrated by examining the diffusive limit of Eq. (5), which results by taking $\psi = 0$ [where we use Eq. (5) with $w_e = 0$, rather than Eq. (7) to allow for latitudinal variations in $\kappa$ and $B$]. By integrating meridionally from the southern

[4]This is consistent with Eq. (15) if $l^{-1}$ is viewed as a measure of the local distance between adjacent extrema in $\tilde{E}(y)$, which are smaller in the tropic.

boundary where the diffusive flux is zero, we obtain

$$\frac{dS}{dy} = -\frac{S_0}{\kappa B h} F(y). \tag{17}$$

Here, we have introduced the northward freshwater transport carried by the atmosphere and rivers

$$F(y) \stackrel{\text{def}}{=} \int_{y_s}^{y} B(y')\tilde{E}(y')\, dy', \tag{18}$$

where $y_s$ is the southern domain limit. Equation (17) shows that the extrema in $S(y)$ are co-located with the zeros of $F(y)$. The extrema in $\tilde{E}$, on the other hand, are found where $d\tilde{E}/dy = 0$ and thus co-located with zeros of $d^2F/dy^2$ (assuming a constant basin width $B$). For the single wavenumber cosine $\tilde{E}$ field, the zeros of $F$ and $d\tilde{E}/dy$ are co-located and the $\tilde{E}$–$S$ curve is a straight line that does not cross itself. However, for the symmetric "Atlantic-like" $\tilde{E}$ field, the zeros of $F(y)$ in the subtropics (at $|y| \approx 0.33$) are located poleward of the zeros of $d\tilde{E}/dy$ (at $|y| \approx 0.28$). The observed atmospheric freshwater transport also shares this feature (see Figs. 1a and 8b). Thus, bending and looping in $\tilde{E}$–$S$ curves can be caused by both advective and diffusive transport for net evaporation fields composed of multiple wavenumbers.

Figure 7b shows how advection modifies the diffusive $\tilde{E}$–$S$ relations for a Peclet number of 2. The northward advection shifts the salinity extrema northward of the extrema in net evaporation. In the northern subtropics, this reinforces the poleward displacement of the salinity maximum relative to the net evaporation maximum arising from the diffusive salt transport and amplifies the loop of the $\tilde{E}$–$S$ curve in the northern subtropics. In the southern subtropics, the displacing tendencies due to diffusion and advection counter each other, which essentially removes the loop in the $\tilde{E}$–$S$ curve.

Figure 6b shows the model $\tilde{E}$–$S$ relations area-averaged in subpolar and subtropical latitude bands. In correspondence with the observational analysis (Fig. 3), the subtropical regions extend from the equator to the latitude where net evaporation changes from being positive to negative (at $|y/L| = 0.7$) and the subpolar regions extend poleward from this point to $|y/L| = 1$. As the the diffusive solution is equatorially symmetric, this area-averaged representation yields only two points in the $\tilde{E}$–$S$ diagram: One subpolar and one subtropical that are connected by a straight line. The advective solution, on the other hand, yields four different points in the $\tilde{E}$–$S$ plane that do not fall on a straight line. Compared to the Atlantic data in Fig. 3, the model has a more pronounced northward salinity gradient across the equator. Thus, effects of the meridional advection persists in the coarse-grained $\tilde{E}$–$S$ relation of the conceptual model: moving from the south to the north, the $\tilde{E}$–$S$ curve turns anticlockwise. This advective signature is not apparent in Fig. 3. However, as we will discuss in Section 4c, Fig. 6b qualitatively resemble the $\tilde{E}$–$S$ relation obtained when the Atlantic salinity is vertically averaged over the upper kilometre.

### *c. Solutions for equatorially asymmetric net evaporation fields*

We now consider how hemispheric asymmetries of the $\tilde{E}$ fields affect the model salinity solutions. We will first consider the diffusive limit, where the basin widths only indirectly affect the solutions, and then consider some advective-diffusive solutions. For this purpose, we construct semi-realistic representations of the Atlantic and Indo–Pacific net evaporation fields in "model basins" that extend from 65°S to 65°N, divided zonally in the Southern Ocean according to the standard hydrographic definitions (Zweng et al. 2013). As in section 2, the net evaporation data are taken from the ERA-Interim reanalysis for 1979–2012 (Dee et al. 2011) and include continental runoff (Wills and Schneider 2015). Within the basin sectors, we first compute the area-mean net evaporation over the basins; about 0.17 and -0.06 m year$^{-1}$ for the Atlantic and Indo–Pacific sectors, respectively. Next, we subtract these numbers from the zonal-mean net evaporation fields, which are then integrated northward from 65°S yielding the freshwater transport $F(y)$ in each basin sector; see Eq. (18). The calculation yields freshwater transports that are zero at both the southern and northern "basin boundaries", allowing us to ignore issues related to freshwater transports into the Arctic Ocean (Wijffels et al. 1992; Talley 2008) and imposing a boundary condition of zero diffusive flux at both of the latitudinal basin boundaries when Pe = 0. (We will briefly discuss the impact of the net evaporation over the Atlantic sector in the next section.)

Figure 8 shows the latitudinal variation of the basin widths as well as the freshwater transport per basin width, defined as

$$G(y) \stackrel{\text{def}}{=} F(y)/B(y), \tag{19}$$

where $B(y)$ is the zonal width of the basin sector. Note that in the diffusive limit, the salinity solutions depend on the basin width only because of its effect on $G(y)$; see Eqs. (17,20). In the tropics the Indo–Pacific basin is roughly five times as wide as the Atlantic basin, but the difference decreases northward. The transports per unit width, on the other hand, are broadly similar in amplitude, but with some structural differences between the basins caused by large-scale zonal asymmetries in the net evaporation and drainage basins (Wills and Schneider 2015; Craig et al. 2017). The similarity in the amplitudes of $G$ primarily reflects that the amplitudes of the zonal-mean net evaporation in the two basins are broadly similar (Fig. 1). As we will show it is primarily the difference in shape between the Atlantic and Indo–Pacific freshwater transports, rather than the difference in their amplitudes, that is the key for the basin difference in surface salinity.

In the diffusive limit (Pe = 0), the salinity field can be obtained by integrating Eq. (17) northward from the southern boundary. Taking $\kappa$ as constant one obtains

$$S(y) = -\frac{S_0}{\kappa h} \int_{y_s}^{y} G(y')\, dy', \tag{20}$$

where the salinity at the southern boundary has been set to zero. Figure 9a shows the diffusive salinity solutions in the "Atlantic" and "Indo–Pacific" sectors. Here, we have taken $\kappa h = 1.5 \cdot 10^6$ m$^3$ s$^{-1}$ to obtain realistic salinity variations. For a surface layer with a thickness of about 100 m, this translates to an effective diffusivity $\kappa$ of order $10^4$ m$^2$ s$^{-1}$; we will discuss the realism of this number below. We emphasise that the value of $\kappa h$ only affects the amplitude of the salinity fields and not their shape, which are determined by the shape of $G$.

It is relevant to note that $\kappa$, which in the model represents an effective diffusivity associated with meso-scale eddies and wind-driven gyres, is in reality expected to have latitudinal variations. Scaling arguments suggest that diffusivity due to wind-driven gyres is proportional to the square of the wind-stress curl (Wang et al. 1995; Rose and Marshall 2009), and hence has peaks at the latitudes where the transports of the tropical, subtropical, and subpolar gyres have their maxima. Further, meso-scale eddy diffusivity tends generally to decline poleward and has a local minimum near the equator (Abernathey and Marshall 2013). For simplicity, we will here take the diffusivity $\kappa$ to be constant in our calculations. However, we can qualitatively infer how latitudinal variations in $\kappa$ would affect our results in the diffusive limit: By inspecting Eq. (17), we see that a locally higher/lower $\kappa$ gives a lower/higher salinity gradient. We also note that in the diffusive limit, variations in $\kappa$ cannot shift the extrema of the salinity field, which locations occur where $F(y) = 0$.

In Fig. 9a the "Atlantic" solution is broadly similar to the observations, whereas the "Indo–Pacific" solution has a too pronounced northward decrease in salinity. In the calculation, the ocean physics (i.e., $\kappa h$) is identical in the two "basins" implying that the differences in the salinity fields are caused only by the difference in freshwater forcing. Figure 9a also shows the salinity solutions associated with the antisymmetric and symmetric parts of $G$, respectively. It is the stronger inter-hemispheric freshwater transport per basin width (related to the equatorially-symmetric part of $G$) in the Indo–Pacific that creates its greater south-to-north salinity difference. Physically, this results from inter-hemispheric moisture transport, in part associated with the Asian Monsoon system (Emile-Geay et al. 2003; Wills and Schneider 2015; Craig et al. 2020). The symmetric salinity fields are fairly similar in the two basin sectors, reflecting that the equatorially symmetric parts of the net evaporation fields are roughly similar but somewhat stronger in the Atlantic.

The difference in salinity between the northern and southern ends of the basin is proportional to the integral of $-G(y)$ over the entire basin (Eq. 20). Essentially, this integral measures the equatorial asymmetry of the $\tilde{E}$ field and is positive if the centre of mass of $\tilde{E}$ is the northern hemisphere. In the calculation, the north–south salinity difference is 1 and -2.6 psu in the Atlantic and Indo–Pacific sectors, respectively. This reflects the larger length scales, or lower wavenumbers, of the symmetric part of $G$ in the Indo–Pacific that are more weakly damped by the diffusive transport. Thus, in the diffusive model the differences in the net evaporations fields between the basins alone give a salinity difference between the two basins in the north that is roughly comparable to the observations.

Figure 10 shows the $\tilde{E}$–$S$ digrams for the diffusive model solutions (Fig. 9a). In the Atlantic, the diffusive model reproduces several qualitative features of the observations. In the Indo–Pacific, the $\tilde{E}$–$S$ relation of the diffusive model deviates more from the observations because of the stronger northward decline of salinity in the model. In the Atlantic, $\tilde{E}$–$S$ curve make loops in the subtropics, reflecting the salinity maxima [found where $F(y) = 0$, see Eq. (17)] are located poleward of the net evaporation maxima. The regression slope (Eq. 2) is about 40% steeper in the ”Indo–Pacific” than in the ”Atlantic”. Thus, the larger spatial scales of the ”Indo–Pacific” freshwater forcing amplifies the sensitivity of the surface salinity. We have also calculated a $\tilde{E}$–$S$ diagram using subtropical and subpolar latitude bands for the diffusive model solution (not shown): In the ”Indo–Pacific”, the subtropical and northern subpolar points fall approximately on a straight line, qualitatively resembling the observations shown in Fig. 3; the larger cross-equatorial salinity gradient in the Atlantic model solution causes greater differences between the model and the observations.

Interestingly, in the diffusive limit the equatorially asymmetric freshwater transports (Fig. 8b) yield $\tilde{E}$–$S$ relationships that resemble the observational relationships in Fig. 2, particularly in the Atlantic. However, the advective-diffusive solution with an equatorially-symmetric net evaporation field, also gives a $\tilde{E}$–$S$ curve (Fig. 7b) that captures qualitative aspects of the Atlantic $\tilde{E}$–$S$ curve in observations. Thus, it is relevant to examine combined effects of northward advection and equatorially asymmetric forcing on the Atlantic $\tilde{E}$–$S$ relationships in the model. For this purpose, we have calculated advective-diffusive solution to Eq. (5) using the Atlantic basin width and freshwater transport shown in Fig. 8. As detailed in the appendix, the vertical mixing term (proportional to $w_e$) is neglected and the upper layer volume transport ($\psi = vhB$) and $\kappa h$ are taken to be constant. As the basin width varies, the meridional velocity $v$ varies and the Peclet number (Eq. 13) can be written as

$$\mathrm{Pe}(y) = \frac{\psi}{\kappa h} \frac{L}{B(y)}, \tag{21}$$

where $L$ ($\sim$ 7000 km) is the distance from the equator to the northern basin boundary. Figure 9b shows "Atlantic" advective-diffusive solutions for $\psi/(\kappa h) = 1$ and $\psi/(\kappa h) = 2$. Since $L/B$ is approximately one in the Atlantic (see Fig. 8a), these solutions correspond roughly to Peclet numbers of 1 and 2, respectively; although the local Peclet numbers are higher in the more-narrow northern part of the basin. Stronger advection increases the damping, which causes the salinity range to decrease with increasing Peclet number. Comparison to the solutions calculated with equatorially symmetric freshwater forcing (dash-dotted lines in Fig. 9b) reveal that asymmetric forcing and northward advection reinforce each other to shift the extrema in the salinity field northward. Figure 11 shows the $\tilde{E}$–$S$ relationships for the advective-diffusive Atlantic solutions with realistic net evaporation. The diffusive Pe = 0 and the Pe $\approx$ 1 solutions share several qualitative features, but the advection enhances the subtropical loops in the north and decreases them in the south. The northward advection also increases the inter-hemispheric salinity contrast and the

$\tilde{E}$–$S$ digram for the solution with stronger advection (Pe $\approx 2$) gives, qualitatively, a worse fit to the Atlantic observations. Thus, the $\tilde{E}$–$S$ relationship of the model qualitatively resembles Atlantic observations best in the diffusive limit, or for Peclet numbers smaller than one; note that the regression slopes are somewhat closer to the observations in Fig. 10 than in Fig. 11. As will be discussed below, however, the observed Atlantic zonal-mean relationship between the net evaporation and the mean salinity in the upper kilometre qualitatively resembles model solutions with a Peclet number on the order of unity.

We underline that the Atlantic Basin has a fairly uniform zonal width. In the Atlantic, the simpler model with constant basin width (Eq. 7, Fig. 7) gives advective-diffusive solutions that are very similar to the ones of the model that accounts for varying basin width (Eq. A9, Fig. 9). In the Indo–Pacific, on the other hand, a constant northward volume transport affects the model salinity field more strongly in the northern extra tropics, where the basin is narrower and the local Peclet number higher (not shown). Furthermore, since the Indo–Pacific is wider than the Atlantic, the same northward overturning volume transport would correspond to a smaller Peclet number in the Indo–Pacific: the associated weaker northward salt advection is one factor that should favour northern sinking in the narrower Atlantic over northern sinking in the wider Indo–Pacific (Jones and Cessi 2017).

Summarising some key results of the conceptual model analyses, we note that the limit of diffusive salt transports yields $\tilde{E}$–$S$ relationships that reproduce the main qualitative features of the observations. These features include a general higher salinity sensitivity to net evaporation variations in the Indo–Pacific and subtropical loops in the $\tilde{E}$–$S$ curves. The higher Indo–Pacific sensitivity is due to the larger inter-hemispheric asymmetry in the $\tilde{E}$ field, which is associated with low wavenumbers (large meridional scales) that are weakly damped in the model. A northward advection can create or enhance subtropical loops of the observed orientation (anticlockwise progressing poleward from the equator) in the northern hemisphere, but acts to suppress such loops due to diffusive transport in the southern hemisphere. Thus, the model results do not suggest a dominat role of northward near-surface advection in shaping the observed Atlantic $\tilde{E}$–$S$ relationship. However, the poleward surface Ekman transport in the subtropics, which is essentially symmetric with respect to the equator, could reinforce the subtropical loops in both hemispheres similar to the (northward) advective enhancement of norther loops seen in the conceptual model.

## 4. Understanding observations based on the conceptual model

We now go on to further discuss the observed $\tilde{E}$–$S$ relations (Figs. 2,3) in the light of the insights from the conceptual model. We first discuss some general features of the $\tilde{E}$–$S$ curves and then proceed to consider signatures of the Atlantic Meridional Overturning Circulation.

### *a. Is the salt transport in the near-surface ocean diffusive?*

The purely diffusive model calculations with realistic forcing reproduce two salient features of the observed $\tilde{E}$–$S$ relations (Fig. 2): they have weaker slopes in the tropics than in the extratropics and they turn anticlockwise progressing poleward from the equator, generally forming loops. In the model, where the horizontal diffusivity is constant, it is the relative narrowness of the wet near-equatorial latitude bands that give $\tilde{E}$–$S$ curves with weaker tropical slopes: the tropical net evaporation field has locally a higher curvature that causes a stronger diffusive damping of the salinity field (Eq. 15). The loops of the $\tilde{E}$–$S$ curves in the subtropics occur because the salinity maxima are located poleward of the maxima in net evaporation. In the diffusive limit of the conceptual model, the relative location of these maxima is controlled by the spatial structure of the net evaporation. Notably, the observed net evaporation yields diffusive solutions with salinity maxima shifted poleward of the $\tilde{E}$ maxima. For the cosine evaporation field (Eq. 8, Fig. 4), on the other hand, the salinity extrema of the diffusive solution are co-located with the extrema in $\tilde{E}$. It would also be possible to construct net evaporation fields that yield a diffusive solution with the salinity maxima equatorward of the subtropical maxima in net evaporation.

In the diffusive model calculation (Fig. 10), we use $\kappa h = 1.5 \cdot 10^6$ m$^3$ s$^{-1}$ to get a realistic salinity range. In the tropics, surface salinities are representative of the vertical-mean salinity in a relatively thin upper layer of about 100 m (see Fig. 12), which would imply an effective diffusivity $\kappa$ of about $1.5 \cdot 10^4$ m$^2$ s$^{-1}$ in the surface ocean. This magnitude of $\kappa$ is about a factor of 3 larger than the zonal-mean of the estimated meso-scale eddy diffusivities in the tropics (Abernathey and Marshall 2013), but similar to estimated local peak values in eddy diffusivities (Zhurbas and Oh 2004; Abernathey and Marshall 2013). Zonal shears associated with the wind-driven gyres serve to enhance the meridional diffusivity acting on the zonal-mean salinity (Rhines and Young 1983; Young and Jones 1991; Wang et al. 1995; Rose and Marshall 2009), which may partly rationalise the high value of $\kappa$ used in the conceptual model[5]. It is also possible that the large model diffusivity compensates for salinity damping processes such as vertical mixing that are not included in the model.

Advection is another mechanism that can shift salinity extrema downstream of net evaporation extrema, irrespective of the details of the net evaporation field (Fig. 5). Gordon et al. (2015) proposed that the poleward shifts of the salinity maxima relative to those in net evaporation are primarily caused by the wind-driven surface Ekman flows, which are directed poleward in the trade-wind belt equatorward of about 30° latitude. However from the zonal-mean $\tilde{E}$–$S$ relation alone, it is not possible to determine the relative importance of advective and diffusive processes in displacing the maxima in salinity and net evaporation. As noted in section 3.1, estimates of

[5]In diffusive energy balance models, thermal ocean diffusivities, which accounts for wind-driven gyres, are typically on the order of $10^5$ m$^2$ s$^{-1}$ (Rose and Marshall 2009).

surface Ekman velocities and eddy diffusivities in the tropics suggest a Peclet number of about 4 (Eq. 13), indicating that advection is stronger than diffusion. This is in line with the study of Busecke et al. (2017), who found that near the subtropical surface salinity maxima horizontal eddy diffusion only balances a smaller fraction (10–30 %) of the local evaporative surface forcing. With an effective meridional diffusivity on the order $1.5 \cdot 10^4$ m$^2$ s$^{-1}$, as suggested by the diffusive model calculations, the Peclet number becomes close to or lower than one. Thus, it is possible that horizontal diffusive transports due to wind-driven gyre circulations is of leading-order importance for shaping the zonal-mean surface salinity field near the subtropical salinity maxima, despite horizontal eddy diffusion being of secondary importance for the local salinity balance (Busecke et al. 2017).

### *b. Effects of vertical mixing*

The damping due to horizontal advection and diffusion decreases with increasing spatial scales. These scale-dependent damping processes are likely too weak to control the surface salinity variations at the largest spatial scales, where vertical mixing should become more important. This is indicated by the diffusive calculation (Fig. 9a), where the ”Indo–Pacific” solution has a north-south salinity difference that is too large compared to observed salinity variations. This reflects the weak diffusive damping of forcing at low wavenumbers.

A simple representation of vertical mixing is to assume that it restores the surface salinity towards a subsurface salinity with an inverse timescale $r = w_e/h$; see Eq. (5). Adding this vertical mixing term in Eq. (7) and neglecting advection, we obtain

$$rS = \kappa \frac{d^2 S}{dy^2} + S_0 \tilde{E}/h. \tag{22}$$

The horizontal length scale at which vertical mixing becomes comparable to horizontal diffusion is roughly

$$L_{\kappa r} \sim \sqrt{\kappa/r}. \tag{23}$$

When the length scale of the forcing is much larger than $L_{\kappa r}$, vertical mixing will dominate the salinity damping. If we assume that the vertical mixing is due to vertical diffusion, with a diffusivity $K_z$ and acting on a salinity structure with a vertical length scale $h$, then $r \sim K_z/h^2$. Equation (23) can thus be written as

$$L_{\kappa r} \sim h\sqrt{\kappa/K_z}. \tag{24}$$

In the upper ocean, $K_Z$ typically ranges from $10^{-5}$ m$^2$ s$^{-1}$ in the thermocline (Ledwell et al. 1998) to $10^{-4}$ m$^2$ s$^{-1}$ just below the surface mixed layer (Large et al. 1994; Cronin et al. 2015). Taking $h \sim 100$ m, $K_z = 0.5 \cdot 10^{-4}$ m$^2$ s$^{-1}$, and $\kappa$ in the range $10^3$ to $1.5 \cdot 10^4$ m$^2$ s$^{-1}$, gives values of $L_{\kappa r}$ in the range from 500 to 1700 km. Accordingly, vertical mixing should dominate over horizontal diffusion in the damping of the near surface salinity at scales above a few 1000 km.

In the diffusive calculation (Fig. 9a), the spatial-mean net evaporation over the basin sectors was removed. If the basin-mean net evaporation is retained in the calculations, there will be a corresponding uniform diffusive salinity divergence and salt export at the boundaries to balance the freshwater loss. As this spatially-uniform forcing has virtually an infinite length scale, the diffusive response entails basin-scale gradients associated with large salinity variations. Specifically, including the mean Atlantic freshwater loss of 0.17 m year$^{-1}$ in the calculation, the north–south Atlantic salinity difference grows from 1 to 12 psu. This further indicates that the forcing of the surface salinity due to variations in the surface freshwater flux on inter-hemispheric to inter-basin scales are countered by vertical mixing rather than horizontal diffusion or advection.

### c. Signatures of the Atlantic Meridional Overturning Circulation

The Atlantic surface salinity is fairly symmetric with respect to the equator, but as shown in Fig. 12, the Atlantic salinity is more equatorially asymmetric at depth. Presumably, this reflects the vertical structure of the meridional flow in the Atlantic. Near the surface, the zonal-mean meridional flow is roughly symmetric around the equator and primarily controlled by wind-driven Ekman transport (Gordon et al. 2015). The Atlantic Meridional Overturning Circulation (AMOC), on the other hand, has a relatively weak impact on the near-surface flow but yields a vertical-mean northward flow in the upper kilometer of the basin (Wunsch and Heimbach 2013; Cessi 2019). Near the surface, the latitude bands with alternating meridional flow directions and enhanced zonal-mean diffusivity due to wind-driven gyres and shallow overturning cells are likely to reduce the advective signature of the AMOC on the salinity field.

Figure 13 shows the Atlantic and Indo–Pacific $\tilde{E}$–$S$ relationships that result when the zonal-mean salinity is based on the vertical average from the surface down to 1000 m, rather than on the surface salinity. Note that the net evaporation is the same as used in Fig. 2. The shapes of the $\tilde{E}$–$S$ relationships are similar for vertical salinity averages taken in the upper 500 to 1000 m, but the range of salinity variation decreases when the averaging depth range is increased. The deeper Atlantic $\tilde{E}$–$S$ relation has a magnified subtropical loop in the northern hemisphere, whereas the loop in the southern hemisphere is diminished. This is qualitative consistent with the effect of northward advection in the conceptual model, which can be seen by comparing advective-diffusive solutions in Figs. 7b and 11 with diffusive solutions in Figs. 7a and 10. Thus, the deeper Atlantic $\tilde{E}$–$S$ relation appears more advective and departs from the diffusive model solution (Fig. 10). In the Indo–Pacific the surface and depth-averaged $\tilde{E}$–$S$ relations remain qualitatively similar.

We note that the largest poleward shift of the surface salinity maximum relative to the net evaporation maximum is found in the subtropical North Atlantic. In Fig. 2 this manifested in a more pronounced loop of the $\tilde{E}$–$S$ curve in the North Atlantic than in the South Atlantic. Northward advection due to the AMOC may play a role here; in the tropical Atlantic, the AMOC and the subtropical cells interact and yield a poleward near surface flow that is stronger in the northern than in the southern hemisphere (Fratantoni et al. 2000; Schott et al. 2013): In the ECCO ocean reanalysis, the zonally-integrated Atlantic poleward volume transport in the upper 50 m is about twice as strong at 15°N as it is at 15°S (see Figs. 1 and 2 in Wunsch and Heimbach 2013). Thus, the conceptual model results suggest that an enhancement of the zonal-mean near surface advection due to the AMOC influences the $\tilde{E}$–$S$ relationship in the subtropical North Atlantic.

## 5. Discussion and conclusion

We used diagrams relating net evaporation and salinity to examine how atmospheric and oceanic processes shape the zonal-mean salinity in the Atlantic and Indo–Pacific. Diagrams based on observations yield curves in the $\tilde{E}$–$S$ plane that have some common as well as different characteristics in the two basins, indicating a higher salinity sensitivity to net evaporation variations in the Indo–Pacific than in the Atlantic (Figs. 2, 3, 13). To interpret the observations, we examined a conceptual advective-diffusive model. Our main findings include:

1. The zonal-mean salinity field in the upper ocean (~100–150 m) appears be primarily controlled by meridional diffusive transport created by mesoscale- and gyre-scale ocean eddies as well as shallow subtropical overturning cells. The effective meridional diffusivity inferred from the conceptual model is on the order of $10^4$ m$^2$ s$^{-1}$.

2. The poleward shift of the surface salinity maxima relative to the net evaporation maxima in the subtropics can be caused by either diffusive or advective transport; the $\tilde{E}$–$S$ diagram alone cannot determine which process dominates.

3. The larger spatial scales associated with the inter-hemispheric asymmetry in the Indo–Pacific net evaporation field may be as important for creating the low surface salinities in the northern basin as the local net evaporation rate.

4. The Atlantic depth-averaged $\tilde{E}$–$S$ relation (Fig. 13) shows a greater signature of advection than the Atlantic surface relation, which appears to be shaped by diffusive transport (point 1 above).

The present work has been motivated by the question of why the surface salinities are higher in the North Atlantic than in the North Pacific. Specifically, the question of whether it is primarily atmospheric or oceanographic processes that create the salinity contrast. In the literature, the high Atlantic surface salinity has frequently been interpreted as a sign of a salt advection feedback, which is associated with the AMOC (Ferreira et al. 2018; Weijer et al. 2019). However, the observed Atlantic zonal-mean relationship between net evaporation and surface salinity does not exhibit a clear signature of northward mean advection. Indirectly, the AMOC may still be important for the North Atlantic surface salinities by carrying saline Indian Ocean thermocline water northward at depth (Gordon 1986; Rahmstorf 1996; Beal et al. 2011).

The asymmetry in net evaporation between the Atlantic and the Pacific (and also the Indo–Pacific) is clearly important for the northern subpolar basin difference in surface salinity. Modelling studies indicate that if the present-day surface freshwater forcing pattern is amplified, the salinity difference between the North Atlantic and the North Pacific increases, and so does the AMOC (Cael and Jansen 2020). Some studies on the role of the net evaporation have emphasized local differences in subpolar regions (Warren 1983; Emile-Geay et al. 2003), whereas others have emphasized basin-integrated differences (Weyl 1968; Rahmstorf 1996). The present idealized diffusive model calculations show that, even in a basin sector with zero mean net evaporation, hemispheric asymmetries in the net evaporation field can cause a significant north–south salinity gradient. The fact that the center of mass of the net evaporation is shifted south of the equator in the Indo–Pacific sector acts to lower surface salinities in the north relative to the south, where the Antarctic Circumpolar Current serves to keep the Southern Ocean surface salinities almost zonally uniform (see Fig. 1b and Marshall and Speer 2012). Notably, Emile-Geay et al. (2003) argued that atmospheric freshwater transport due to the Asian Monsoon is crucial for creating subpolar net precipitation rates that are higher in the North Pacific than in the North Atlantic (Craig et al. 2017, 2020). With a scale-dependent damping of the surface salinity, a larger meridional fetch of the subpolar precipitation will depress the local surface salinity more. This underlines that it is not only the local precipitation rates that matter: Surface freshwater forcing with low meridional wavenumber, for example, due to the Asian Monsoon and other large-scale atmospheric circulation patterns in the Indo–Pacific sector (Wills and Schneider 2015; Craig et al. 2020), are a significant factor for the low surface salinities in subpolar North Pacific. Ultimately, the importance of the low wavenumber evaporative forcing on the surface salinity is determined by the relative strengths of horizontal advective-diffusive transports and vertical mixing [see Eq. (23)].

It is relevant to ask if the effective meridional diffusivities are different in the North Atlantic and North Pacific and hence may contribute to the basin asymmetry in surface salinity. In fact, estimated subpolar mesoscale-eddy diffusivities are higher in the North Atlantic, particularly when comparing the central and eastern subtropical gyres: eddy diffusivities are typically a factor of two larger in the North Atlantic (Zhurbas and Oh 2004; Abernathey and Marshall 2013). Simple models of meridional diffusive transport due to wind-driven gyres suggest that the effective diffusivity increases with basin width (Wang et al. 1995; Rose and Marshall 2009), which in turn suggests that the gyres should accomplish a larger meridional salt transport in the wider Indo–Pacific than in the narrower Atlantic. However, the North Pacific narrows significantly northward and is as narrow as the North Atlantic at 55°N (Fig. 8a). Thus, the widths of the northern subpolar gyres are fairly similar in the two basins. Furthermore, the tilted zero wind-stress curl line and its temporal migrations in the North Atlantic are two factors that serve to enhance meridional salt transport carried by wind-driven gyres (Warren 1983; Seager et al. 2002; Czaja 2009); these features may be more important than a relatively small difference in basin widths for the surface-salinity difference.

Ferreira et al. (2018) attempted to assess the relative importance of atmospheric and oceanic processes in setting the subpolar surface salinity difference of ~ 2 psu between the North Atlantic and North Pacific by analysing a $\tilde{E}$–$S$ diagram[6] divided in subtropical and subpolar latitude bands. Arguing that the slopes of the regression lines are controlled by oceanic processes and that the difference in basin-mean salinity is created by comparable contributions from surface freshwater forcing and inter-ocean salt transport, they proposed that atmospheric and oceanic processes both contribute to the present-day Atlantic–Pacific surface salinity asymmetry. The present analysis of $\tilde{E}$–$S$ diagrams divided in finer latitude bands does not alter this general conclusion: the ratios of the Indo–Pacific and Atlantic regression slopes are similar in both types of diagrams. Furthermore, the qualitative conclusion is not sensitive to whether only the Pacific or the combined Indo–Pacific basin is used in the analysis. However, the conceptual model shows that the regression slopes (Eq. 15) can be influenced by the structure of the atmospheric freshwater forcing. If the difference of the Atlantic and Indo–Pacific regression slopes primarily reflects structural differences of the freshwater forcing, one could argue for a larger dominance of atmospheric processes in setting the Atlantic–Pacific asymmetry in surface salinity.

[6]Their Fig. 4 that is comparable to the present Fig. 3

*Acknowledgments.* We thank Paola Cessi for interesting discussions and valuable comments on this work.

*Data availability statement.* All data used here are available from the references given in the text.

## APPENDIX

Here, we provide details on how solutions to the conceptual model can be obtained. We also discuss the boundary condition of zero diffusive flux at the northern model boundary: how it affects the salt flux at the southern model boundary and how this can be interpreted physically.

To begin with, we outline how a solution to Eq. (7) can be obtained for a general forcing $\tilde{E}(y)$ in domain extending from $y = -L$ to $y = L$. We consider $\tilde{E}$ fields that integrate to zero over the domain, and seek solutions that in the diffusive limit have zero diffusive flux at the boundaries. In this case, the forcing can be represented by the following Fourier series (cf. Arfken 1985)

$$\tilde{E}(y) = \sum_{n=1}^{\infty} [\hat{E}_n^c \cos(l_n y) + \hat{E}_n^s \sin(k_n y)], \tag{A1}$$

where $l_n = n\pi/L$ and $k_n = (n - 1/2)\pi/L$ are n:th wavenumbers and $\hat{E}_n^c$ and $\hat{E}_n^s$ are Fourier coefficients, determined by the shape of $\tilde{E}$. Note that the boundary conditions imply that only "odd" sine wavenumbers are included. Following the procedure outlined in section 3 for a single wavenumber, we find that the particular solution to Eq. (7) is given by

$$S_P(y) = \sum_{n=1}^{\infty} [\hat{S}_n^c \cos(l_n y - \phi_n^c) + \hat{S}_n^s \sin(k_n y - \phi_n^s)]. \tag{A2}$$

Here, we have introduced the salinity amplitudes $\hat{S}_n^c$ and $\hat{S}_n^s$ and the phases $\phi_n^c$ and $\phi_n^s$; for the cosine terms these are defined as

$$\hat{S}_n^c \stackrel{\text{def}}{=} \frac{S_0 \hat{E}_n^c \tau_n^c}{h}, \qquad \tau_n^c \stackrel{\text{def}}{=} [(\kappa l_n^2)^2 + (\nu l_n)^2]^{-1/2}, \qquad \tan(\phi_n^c) \stackrel{\text{def}}{=} \frac{\nu}{\kappa l_n}. \tag{A3}$$

The corresponding sine terms are obtain by replacing $\hat{E}_n^c$ and $l_n$ with $\hat{E}_n^s$ and $k_n$ in these expressions.

When the advective velocity $v$ is non zero, the solution given by Eq. (A2) generally has non zero diffusive fluxes at the boundaries, i.e., $dS_P/dy$ is not zero there. The homogeneous solution to Eq. (7), which is $S_H(y) = A + B\exp[\mathrm{Pe}(y/L)]$ (Eq. 16), can be added to satisfy the boundary conditions. As it turns out, Eq. (7) generally lacks solutions that have zero diffusive flux at both boundaries when $v$ is non zero. This can be shown by integrating the equation over the domain; recalling that the integral of $\tilde{E}$ vanishes one obtains

$$v[S(y=L) - S(y=-L)] = \kappa \left(\frac{dS}{dy}\right)_{y=L} - \kappa \left(\frac{dS}{dy}\right)_{y=-L}, \tag{A4}$$

where $S = S_P + S_H$. Thus, when $v$ is non zero the diffusive flux terms on the righthand side can both be zero only if the salinity is the same at the northern and southern boundaries. It is straightforward to show that no solutions exist having zero diffusive fluxes at boundaries when $\tilde{E}(y)$ is equatorially symmetric, which implies that the Fourier series is composed of only cosine terms, i.e. $\hat{E}_n^s = 0$ for all $n$. It then follows from Eq. (A2) that $S_P(y=L) - S_P(y=-L) = 0$ and that the corresponding boundary fluxes ($\kappa dS_P/dy$) are equal, but non zero if $v$ is non zero. The homogenous solution, which includes an exponential term, cannot alone make the lefthand side of Eq. (A4) to vanish; accordingly the diffusive boundary fluxes cannot both be zero for a symmetric $\tilde{E}$ field. There may be special asymmetric $\tilde{E}$ fields that allow the boundary conditions to be satisfied, but no general solution with zero boundary fluxes exits.

For any $\tilde{E}$ field, however, the homogeneous solution (Eq. 16) can be selected to give a vanishing diffusive salt flux at $y = L$: Straightforward algebra shows that the coefficients $A$ and $B$ are given by

$$B = -L\left(\frac{dS_P}{dy}\right)_{y=L} \frac{\exp(-\mathrm{Pe})}{\mathrm{Pe}}, \qquad A = \frac{B}{2\mathrm{Pe}}[\exp(\mathrm{Pe}) - \exp(-\mathrm{Pe})]; \tag{A5}$$

where $\mathrm{Pe} = (vL)/\kappa$ is the Peclet number (Eq. 13), and the constant $A$ has been chosen such that mean upper-layer salinity is zero. The rationale for choosing to satisfy the zero-flux condition at the northern boundary is that the homogenous solution decays away from this boundary. Thus, when the Peclet number is large the zero-flux condition affects the salt field only near the northern boundary, and in the bulk of the domain it is essentially given by the particular solution $S_P(y)$. For intermediate Peclet numbers, this choice gives solutions that reproduce aspects of the Atlantic salinity field (Fig. 6). If instead the homogenous solution is selected to satisfy zero flux at the southern boundary, it grows exponentially northward and gives salt fields that are unrealistic even for moderate Peclet numbers.

The solutions with non zero advection in Figs. 6 and 9 have higher salinities in the north than the south. As the diffusive salt flux at the northern boundary is taken to be zero, Eq. A4 implies that the diffusive flux ($-\kappa dS/dy$) is positive at the southern boundary: salt conservation demands a diffusive flux at the southern boundary balancing the advective salt export from the ”upper ocean” model domain; see Fig. 4. In a more complete model with vertical structure (and in reality), salt is carried from the surface to the interior ocean with the northern sinking, and is returned to the surface with the upwelling in the south. In the upwelling region near the southern boundary, processes such as vertical diffusion and advection are presumably important in the salinity balance. Thus in the conceptual model, the lateral diffusive salt flux across the southern boundary can be viewed as a crude substitute for vertical advective-diffusive transports in a model with an active lower layer.

The homogeneous solution to Eq. (7) can also be used to construct a Green's function $G(y-y')$ (Arfken 1985), which yields the salinity field from the integral

$$S(y) = \frac{S_0}{h}\int_{-L}^{L} G(y-y')\tilde{E}(y')\,dy'. \tag{A6}$$

By using the jump conditions and the zero-flux boundary condition at $y = L$ (Eq. 6), one obtains the following Green's function

$$G(y-y') = 0, \qquad y-y' > 0; \tag{A7}$$

$$G(y-y') = \left(\frac{L}{\kappa}\right)\frac{\exp[\mathrm{Pe}(y-y')/L]-1}{\mathrm{Pe}}, \qquad y-y' < 0. \tag{A8}$$

The salinity fields show in Fig. 6 are obtained by evaluating the integral in Eq. (A6) numerically. In Fig. 6, $\tilde{E}$ is normalised by its maximum absolute value and the salinity fields are normalised and multiplied by $(2\pi)^2$, which implies that a $\cos(2\pi y/L)$ net evaporation field gives a normalised salinity field that ranges between -1 and 1.

Salinity solutions can also be obtained when the basin width $B(y)$ varies by integrating Eq. (5) (with the volume transport $\psi$ constant and the vertical mixing term $w_e = 0$) southward from the norther boundary ($y_n$). This yields

$$\psi[S(y=y_n)-S(y)]-\kappa hB\frac{dS}{dy} = S_0\int_y^{y_n} B(y')\tilde{E}(y')\,dy', \tag{A9}$$

where the condition of zero diffusive flux at $y=y_n$ has been used (Eq. 6). By using the definitions of the freshwater transports $F$ and $G$ (Eqs. 18,19), dividing by $\kappa hB$, and rearranging the terms, one obtains

$$\frac{dS}{dy}-\frac{\psi}{\kappa hB}[S(y)-S(y=y_n)] = -\frac{S_0G(y)}{\kappa h}. \tag{A10}$$

By multiplying Eq. (A10) with the integrating factor $\exp[-\Phi(y)]$ (Arfken 1985), where

$$\Phi(y) \stackrel{\mathrm{def}}{=} \psi\int^y \frac{dy'}{\kappa hB(y')} \tag{A11}$$

we can integrate to obtain the salinity field

$$S(y) = \exp[\Phi(y)]\int_y^{y_n}\exp[-\Phi(y')]\frac{S_0G(y')}{\kappa h}\,dy' + S(y=y_n). \tag{A12}$$

Here $S(y=y_n)$, which affects the spatial mean salinity, can be specified arbitrarily. If $\kappa h$ is constant, the integrating factor can be written as

$$\Phi(y) = \mathrm{Pe}_\psi \int^y \frac{dy'}{B(y')}, \qquad \mathrm{Pe}_\psi \stackrel{\text{def}}{=} \frac{\psi}{\kappa h}. \tag{A13}$$

In this case, the structure of the solutions are determined by the single non-dimensional parameter $\mathrm{Pe}_\psi$, which since $\psi = vhB$ is related to the Peclet number (Eq. 13) as

$$\mathrm{Pe} = \mathrm{Pe}_\psi \frac{L}{B(y)}. \tag{A14}$$

Thus, $\mathrm{Pe}_\psi$ is constant while Pe varies in inverse proportion to the basin width.

## References


Abernathey, R. P., and J. Marshall, 2013: Global surface eddy diffusivities derived from satellite altimetry. *Journal of Geophysical Research: Oceans*, **118 (2)**, 901–916, doi:10.1002/jgrc.20066.

Arfken, G., 1985: *Mathematical Methods for Physicists*. 2nd ed., Academic Press.

Beal, L. M., and Coauthors, 2011: On the role of the Agulhas system in ocean circulation and climate. *Nature*, **472**, 429–436, doi:10.1038/nature09983.

Busecke, J., R. P. Abernathey, and A. L. Gordon, 2017: Lateral eddy mixing in the subtropical salinity maxima of the global ocean. *Journal of Physical Oceanography*, **47 (4)**, 737–754, doi:10.1175/JPO-D-16-0215.1.

Cael, B. B., and M. F. Jansen, 2020: On freshwater fluxes and the atlantic meridional overturning circulation. *Limnology and Oceanography Letters*, **5 (2)**, 185–192, doi:10.1002/lol2.10125.

Cessi, P., 2019: The global overturning circulation. *Annual Review of Marine Science*, **11 (1)**, 249–270, doi:10.1146/annurev-marine-010318-095241.

Cimatoribus, A. A., S. S. Drijfhout, M. den Toom, and H. A. Dijkstra, 2012: Sensitivity of the Atlantic meridional overturning circulation to South Atlantic freshwater anomalies. *Climate Dynamics*, **39 (9)**, 2291–2306, doi:10.1007/s00382-012-1292-5.

Craig, P. M., D. Ferreira, and J. Methven, 2017: The contrast between Atlantic and Pacific surface water fluxes. *Tellus A*, **69 (1)**, 1330 454, doi:10.1080/16000870.2017.1330454.

Craig, P. M., D. Ferreira, and J. Methven, 2020: Monsoon-induced zonal asymmetries in moisture transport cause anomalous Pacific precipitation minus evaporation. *Geophysical Research Letters*, **47 (18)**, e2020GL088 659, doi:10.1029/2020GL088659.

Cronin, M. F., N. A. Pelland, S. R. Emerson, and W. R. Crawford, 2015: Estimating diffusivity from the mixed layer heat and salt balances in the North Pacific. *Journal of Geophysical Research: Oceans*, **120 (11)**, 7346–7362, doi:10.1002/2015JC011010.

Czaja, A., 2009: Atmospheric control on the thermohaline circulation. *J. Phys. Oceanogr.*, **39 (1)**, 234–247, doi:10.1175/2008JPO3897.1.

DeConto, R. M., and D. Pollard, 2003: Rapid Cenozoic glaciation of Antarctica induced by declining atmospheric CO2. *Nature*, **421**, 245–249, doi:10.1038/nature01290.

Dee, D., S. Uppala, A. S. P. Berrisford, P. Poli, and co authors, 2011: The ERA-Interim reanalysis: configuration and performance of the data assimilation system. *Q. J. R. Meteorol. Soc.*, **137**, 553–597, doi:10.1002/qj.828.

Emile-Geay, J., M. A. Cane, N. Naik, R. Seager, A. C. Clement, and A. van Geen, 2003: Warren revisited: Atmospheric freshwater fluxes and ”Why is no deep water formed in the North Pacific”. *Journal of Geophysical Research: Oceans*, **108 (C6)**, doi:10.1029/2001JC001058.

Ferrari, R., M. F. Jansen, J. F. Adkins, A. Burke, A. L. Stewart, and A. Thompson, 2014: Antarctic sea ice control on ocean circulation in present and glacial climates. *Proceedings of the National Academy of Sciences*, **337**, 8753–8758, doi:10.1073/pnas.1323922111.

Ferreira, D., J. Marshall, and J.-M. Campin, 2010: Localization of deep water formation: role of atmospheric moisture transport and geometrical constraints on ocean circulation. *Journal of Climate*, **23 (6)**, 1456–1476, doi:10.1175/2009JCLI3197.1.

Ferreira, D., and Coauthors, 2018: Atlantic-Pacific asymmetry in deep water formation. *Annual Review of Earth and Planetary Sciences*, **46 (1)**, 327–352, doi:10.1146/annurev-earth-082517-010045.

Fratantoni, D. M., W. E. Johns, T. L. Townsend, and H. E. Hurlburt, 2000: Low-latitude circulation and mass transport pathways in a model of the Tropical Atlantic Ocean. *Journal of Physical Oceanography*, **30 (8)**, 1944–1966, doi:10.1175/1520-0485(2000)030<1944:LLCAMT>2.0.CO;2.

Galbraith, E., and C. de Lavergne, 2019: Response of a comprehensive climate model to a broad range of external forcings: relevance for deep ocean ventilation and the development of late cenozoic ice ages. *Climate Dynamics*, **52 (1)**, 653–679, doi:10.1007/s00382-018-4157-8.

Gordon, A. L., 1986: Interocean exchange of thermocline water. *J. Geophys. Res.*, **91 (C4)**, 5037–5046, doi:10.1029/JC091iC04p05037.

Gordon, A. L., C. F. Giulivi, J. Busecke, and F. Bingham, 2015: Differences among subtropical surface salinity patterns. *Oceanography*, **28 (1)**, 32–39, doi:10.5670/oceanog.2015.02.

Hall, A., and S. Manabe, 1997: Can local linear stochastic theory explain sea surface temperature and salinity variability? *Climate Dynamics*, **13 (3)**, 167–180, doi:10.1007/s003820050158.

Haney, R. L., 1971: Surface thermal boundary conditions for ocean circulation models. *J. Phys. Oceanogr.*, **1 (4)**, 241 – 248, doi:10.1175/1520-0485(1971)001<0241:STBCFO>2.0.CO;2.

Hieronymus, M., J. Nilsson, and J. Nycander, 2014: Water mass transformation in salinity–temperature space. *Journal of Physical Oceanography*, **44 (9)**, 2547–2568, doi:10.1175/JPO-D-13-0257.1.

Huisman, S., H. A. Dijkstra, A. S. von der Heydt, and W. P. M. de Ruijter, 2012: Does net E-P set a preference for North Atlantic sinking? *J. Phys. Oceanogr.*, **42 (11)**, 1781–1792, doi:10.1175/JPO-D-11-0200.1.

Jones, C. S., and P. Cessi, 2017: Size matters: Another reason why the Atlantic is saltier than the Pacific. *Journal of Physical Oceanography*, **47 (11)**, 2843–2859, doi:10.1175/JPO-D-17-0075.1.

Jones, C. S., and P. Cessi, 2018: Components of upper-ocean salt transport by the gyres and the meridional overturning circulation. *Journal of Physical Oceanography*, **48 (10)**, 2445–2456, doi:10.1175/JPO-D-18-0005.1.

Large, W. G., J. C. McWilliams, and S. C. Doney, 1994: Oceanic vertical mixing: A review and a model with a nonlocal boundary layer parameterization. *Reviews of Geophysics*, **32 (4)**, 363–403, doi:10.1029/94RG01872.

Ledwell, J. R., A. J. Watson, and C. S. Law, 1998: Mixing of a tracer in the pycnocline. *Journal of Geophysical Research: Oceans*, **103 (C10)**, 21 499–21 529, doi:10.1029/98JC01738.

Maffre, P., J.-B. Ladant, Y. Donnadieu, P. Sepulchre, and Y. Goddéris, 2018: The influence of orography on modern ocean circulation. *Climate Dynamics*, **50**, 1277–1289, doi:10.1007/s00382-017-3683-0.

Marshall, J., and K. Speer, 2012: Closure of the meridional overturning circulation through Southern Ocean upwelling. *Nature Geoscience*, **5**, 171–180, doi:10.1038/ngeo1391.

McCreary, J. P., and P. Lu, 1994: Interaction between the subtropical and equatorial ocean circulations: the subtropical cell. *J. Phys. Oceanogr.*, **24 (2)**, 466–497, doi:10.1175/1520-0485(1994)024<0466:IBTSAE>2.0.CO;2.

Mecking, J. V., S. S. Drijfhout, L. C. Jackson, and T. Graham, 2016: Stable AMOC off state in an eddy-permitting coupled climate model. *Climate Dynamics*, **47**, 2455–2470, doi:10.1007/s00382-016-2975-0.

Nilsson, J., and H. Körnich, 2008: A conceptual model of the surface salinity distribution in the oceanic hadley cell. *Journal of Climate*, **21 (24)**, 6586–6598, doi:10.1175/2008JCLI2284.1.

Nilsson, J., P. L. Langen, D. Ferreira, and J. Marshall, 2013: Ocean basin geometry and the salinification of the Atlantic Ocean. *Journal of Climate*, **26 (16)**, 6163–6184, doi:10.1175/JCLI-D-12-00358.1.

Ponte, R. M., and N. T. Vinogradova, 2016: An assessment of basic processes controlling mean surface salinity over the global ocean. *Geophysical Research Letters*, **43 (13)**, 7052–7058, doi:10.1002/2016GL069857.

Rahmstorf, S., 1996: On the freshwater forcing and transport of the Atlantic thermohaline circulation. *Climate Dynamics*, **12**, 799–811, doi:10.1007/s003820050144.

Reid, J. L., 1961: On the temperature, salinity, and density differences between the Atlantic and Pacific Oceans in the upper kilometre. *Deep Sea Research (1953)*, **7 (4)**, 265 – 275, doi:https://doi.org/10.1016/0146-6313(61)90044-2.

Rhines, P. B., and W. R. Young, 1983: How rapidly is a passive scalar mixed within closed streamlines? *Journal of Fluid Mechanics*, **133**, 133–145, doi:10.1017/S0022112083001822.

Rose, B. E. J., and J. Marshall, 2009: Ocean heat transport, sea ice, and multiple climate states: Insights from energy balance models. *Journal of the Atmospheric Sciences*, **66 (9)**, 2828–2843, doi:10.1175/2009JAS3039.1.

Sarmiento, J. L., and J. R. Toggweiler, 1984: A new model for the role of the oceans in determining atmospheric pCO2. *Nature*, **308**, 621–624.

Schmitt, R. W., 2008: Salinity and the global water cycle. *Oceanography*, **21**, 12–19.

Schott, F. A., J. P. Mccreary Jr., and G. C. Johnson, 2013: *Shallow Overturning Circulations of the Tropical-Subtropical Oceans*, 261–304. American Geophysical Union (AGU), doi:10.1029/147GM15.

Seager, R., D. S. Battisti, J. Yin, N. Naik, N. Gordon, A. C. Clement, and M. A. Cane, 2002: Is the Gulf Stream responsible for Europe's mild winters? *Quarterly Journal of the Royal Meteorological Society*, **128 (586)**, 2563–2586, doi:10.1256/qj.01.128.

Stommel, H. M., 1961: Thermohaline convection with two stable regimes of flow. *Tellus*, **13 (2)**, 224–230, doi:10.1111/j.2153-3490.1961.tb00079.x.

Stouffer, R. J., J. Yin, J. M. Gregory, K. W. Dixon, M. J. Spelman, and co authours, 2006: Investigating the causes of the response of the thermohaline circulation to past and future climate changes. *Journal of Climate*, **19 (8)**, 1365–1387, doi:10.1175/JCLI3689.1.

Talley, L. D., 2003: Shallow, intermediate, and deep overturning components of the global heat budget. *Journal of Physical Oceanography*, **33 (3)**, 530–560, doi:10.1175/1520-0485(2003)033<0530:SIADOC>2.0.CO;2.

Talley, L. D., 2008: Freshwater transport estimates and the global overturning circulation: Shallow, deep and throughflow components. *Progress in Oceanography*, **78**, 257–303, doi:https://doi.org/10.1016/j.pocean.2008.05.001.

Talley, L. D., 2013: Closure of the global overturning circulation through the Indian, Pacific, and Southern Oceans: Schematics and transports. *Oceanography*, **26 (1)**, 80–97, doi:http://www.jstor.org/stable/24862019.

Wang, X., P. H. Stone, and J. Marotzke, 1995: Poleward heat transport in a barotropic ocean model. *Journal of Physical Oceanography*, **25 (2)**, 256–265, doi:10.1175/1520-0485(1995)025<0256:PHTIAB>2.0.CO;2.

Warren, B. A., 1983: Why is no deep water formed in the North Pacific? *Journal of Marine Research*, **41 (2)**, 327–347, doi:10.1357/002224083788520207.

Weijer, W., and Coauthors, 2019: Stability of the Atlantic Meridional Overturning Circulation: A review and synthesis. *Journal of Geophysical Research: Oceans*, **124 (8)**, 5336–5375, doi:10.1029/2019JC015083.

Weyl, P. K., 1968: The role of the oceans in climate change: a theory of the ice ages. *Meteorological Monographs*, **8**, 37–62, doi:10.1007/978-1-935704-38-6{_}4.

Wijffels, S. E., R. W. Schmitt, H. L. Bryden, and A. Stigebrandt, 1992: Transport of freshwater by the ocean. *Journal of Physical Oceanography*, **22 (2)**, 155–162, doi:10.1175/1520-0485(1992)022<0155:TOFBTO>2.0.CO;2.

Williams, P. D., E. Guilyardi, R. T. Sutton, J. M. Gregory, and G. Madec, 2006: On the climate response of the low-latitude Pacific Ocean to changes in the global freshwater cycle. *Climate Dynamics*, **27 (6)**, 593–611, doi:10.1007/s00382-006-0151-7.

Wills, R. C., and T. Schneider, 2015: Stationary eddies and the zonal asymmetry of net precipitation and ocean freshwater forcing. *Journal of Climate*, **28 (13)**, 5115–5133, doi: 10.1175/JCLI-D-14-00573.1.

Wunsch, C., and P. Heimbach, 2013: Two decades of the Atlantic Meridional Overturning Circulation: Anatomy, variations, extremes, prediction, and overcoming its limitations. *Journal of Climate*, **26**, 7167–7186, doi:10.1175/JCLI-D-12-00478.1.

Young, W. R., and S. Jones, 1991: Shear dispersion. *Physics of Fluids A: Fluid Dynamics*, **3 (5)**, 1087–1101, doi:10.1063/1.858090.

Zhurbas, V., and I. S. Oh, 2004: Drifter-derived maps of lateral diffusivity in the pacific and atlantic oceans in relation to surface circulation patterns. *Journal of Geophysical Research: Oceans*, **109 (C5)**, doi:10.1029/2003JC002241.

Zika, J. D., N. Skliris, A. J. G. Nurser, S. A. Josey, L. Mudryk, F. Laliberté, and R. Marsh, 2015: Maintenance and broadening of the ocean's salinity distribution by the water cycle. *Journal of Climate*, **28 (24)**, 9550–9560, doi:10.1175/JCLI-D-15-0273.1.

Zweng, M., and Coauthors, 2013: World Ocean Atlas 2013, volume 2: Salinity. Tech. rep., Natl. Ocean. Data Cent., Silver Spring, MD, 39 pp.

# LIST OF FIGURES

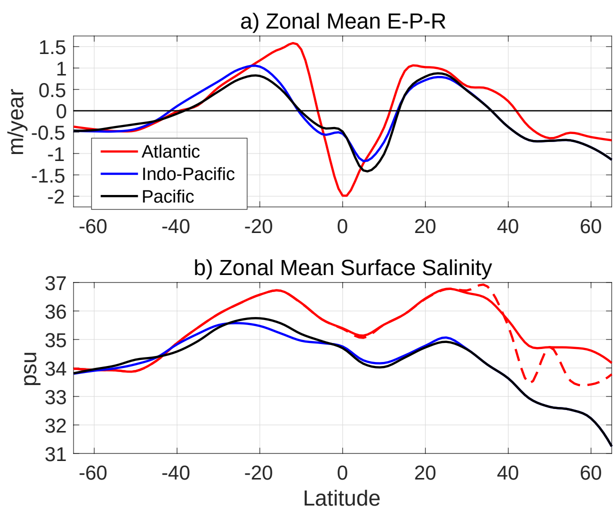


FIG. 1. The zonal-mean net evaporation adjusted for runoff [$\tilde{E}$, see Eq. (1) ] (a) and surface salinity (b) in the Atlantic (red), Pacific (black) and Indo–Pacific (blue) basins, including their marginal seas as defined by the International Hydrographic Organization [basin masks provided in Zweng et al. (2013) are used]. In (b) the solid red line shows the salinity in the open Atlantic, excluding marginal seas, and dashed red line the salinity including the marginal seas: The Black Sea and the Baltic Sea lower the zonal mean salinity of the whole Atlantic Basin, whereas the Mediterranean increases it slightly. In the Pacific and Indo–Pacific Basins, the marginal sea has a negligible influence on the zonal-mean surface salinity. The data have been area-averaged in 5° wide latitude bands. The $\tilde{E}$ is based on ERA-Interim reanalysis for 1979–2012 (Dee et al. 2011), with details on runoff treatment described in Wills and Schneider (2015), and the surface salinity is from the World Ocean Atlas 2013 (Zweng et al. 2013).

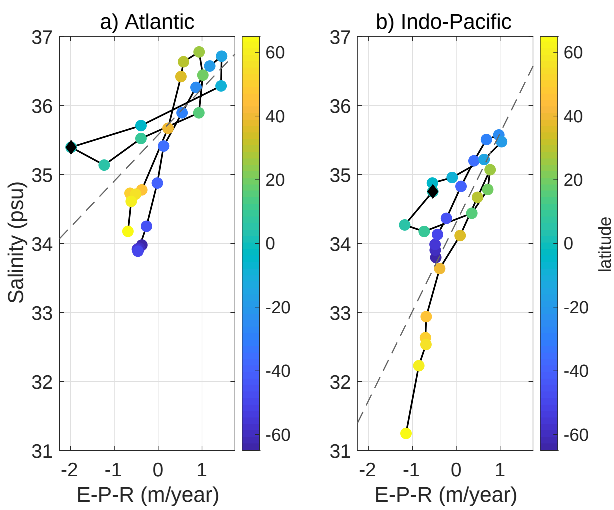


Fig. 2. A representation of the zonal-mean data in Fig. 1 in a diagram with net evaporation (adjusted for river runoff) on the $x$ axis and sea surface salinity on the $y$ axis. Panel a/b shows the Atlantic/Indo–Pacific Basins from 65°S to 65°N. Note in the calculation of the zonal-mean salinity marginal seas are excluded for the Atlantic but included for the Indo–Pacific. The colour scale indicates the latitude and the black marker shows the equator. Dashed lines show regression least square fits (Eq. 2) to the data. The slope in the Atlantic (Indo–Pacific) corresponds to a salinity change of 0.7 (1.3) psu per m year$^{-1}$.

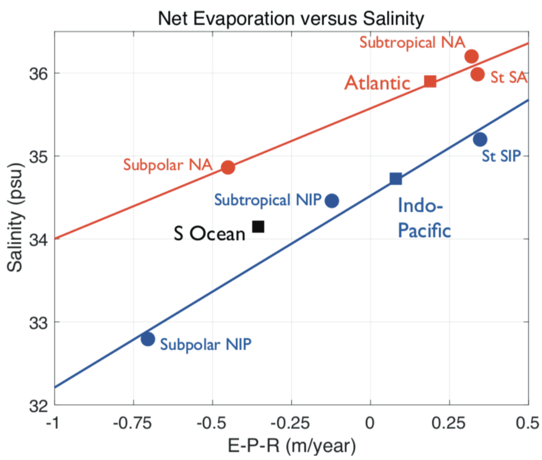


FIG. 3. $\tilde{E}$–$S$ representation of the zonal-mean data in Fig. 1, where the zonal-mean data in the Atlantic (red) and the Indo–Pacific (blue) have been area averaged in subtropical latitude bands (40°S to 0° and 0° to 40°N) and a northern subpolar band (40°N to 65°N). The red and blue squares indicate basin area averages (40°S to 65°N). The solid straight lines show least square fits (Eq. 2) to the area-averaged data. The slope in the Atlantic (Indo–Pacific) corresponds to a salinity change of 1.6 (2.3) psu per m year$^{-1}$. The black square indicate a "Southern Ocean" area average from 65°S to 40°S extending zonally around the globe. The "Southern Ocean" point is located essentially on the Indo–Pacific regression line but further away from the Atlantic one: If including the Southern Ocean in the least square fits, the Atlantic (Indo–Pacific) slope would correspond to a salinity change of 2.1 (2.2) psu per m year$^{-1}$. Thus, the Atlantic Ocean salinity sensitivity implied by this coarser area averaging appears lower than that of the combined Indo–Pacific–Southern Ocean.

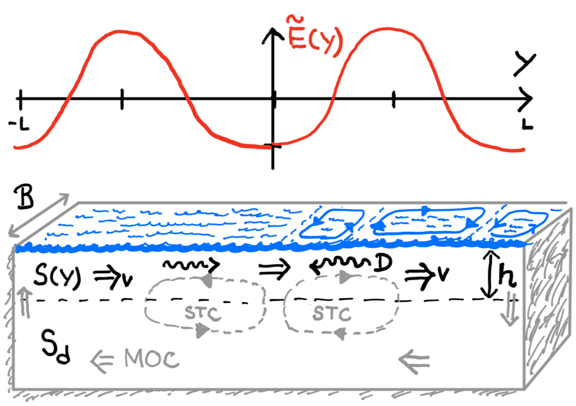


Fig. 4. Sketch of the conceptual model of the zonal-mean salinity $S(y)$ in a surface layer of depth $h$. The salinity is forced by the net evaporation $\tilde{E}(y)$ and damped by meridional advection ($v$) and diffusive transport ($D$); see the text for details. The model does not include the meridional overturning circulation (MOC) in the lower layer and the shallow wind-driven subtropical cells (STCs; see Schott et al. 2013), which are outlined by the grey arrows. The wind-driven horizontal gyre circulation hardly affect the zonal-mean meridional velocity, but their zonal shears enhance the diffusivity of the zonal-mean salinity (Young and Jones 1991; Rose and Marshall 2009). In the northern hemisphere, the tropical, subtropical, and subpolar gyres are indicated by the blue arrows.

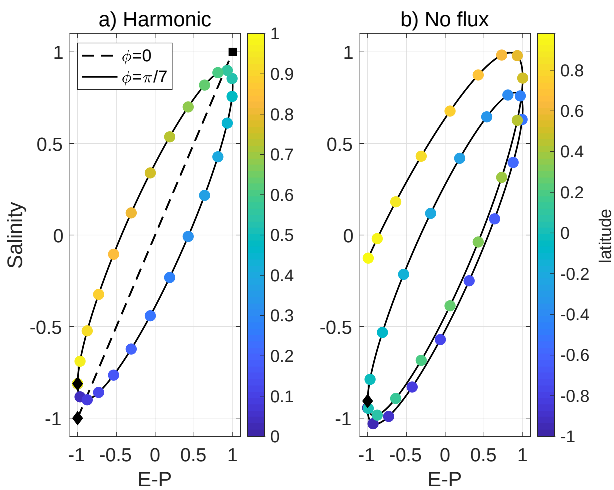


Fig. 5. Relations between net evaporation and salinity for a cosine evaporation field (Eq. 8). The results are presented in non-dimensional form. Panel a shows harmonic solutions, given by Eq. 14, in the diffusive limit ($\phi = 0$ or Pe = 0, dashed line) and for an advective-diffusive case ($\phi = \pi/7$ or Pe $\approx 3$, solid line). The color indicates the latitude ($-1 < y/L < 1$), and the diamond and square markers indicate the equator ($y = 0$) and the subtropical evaporation maximum ($|y/L| = 0.5$), respectively. Panel b shows the $\tilde{E}$–$S$ curve for the salinity solution ($\phi = \pi/7$) where a homogenous solution (Eq. 16) has been added to give zero diffusive salt flux at the northern boundary. Note that for a given $\tilde{E}$ field, the shape of salinity solutions to Eq. (7) depends only on the Peclet number (Eq. 13) and the boundary conditions.

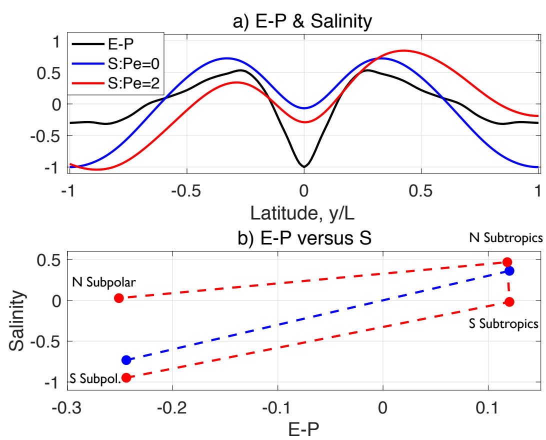


FIG. 6. Salinity solutions obtained from Eq. 7 for a net evaporation field that resembles the equatorially-symmetric Atlantic net evaporation; see the appendix for computational details. Panel a) shows the symmetrized evaporation and salinity solutions for two Peclet numbers that satisfy zero diffusive salt flux at the northern boundary. The results are presented in non-dimensional form. Panel b) shows a $\tilde{E}$–$S$ diagram in which the data in a) has been area-averaged in subpolar ($0.7 < |y/L| < 1$) and subtropical ($0 < |y/L| < 0.7$) latitude bands. The dashed lines connect the area-averaged values. In the diffusive case with $\mathrm{Pe} = 0$, the salinity fields is equatorially symmetric and the area averaging yield only two points.

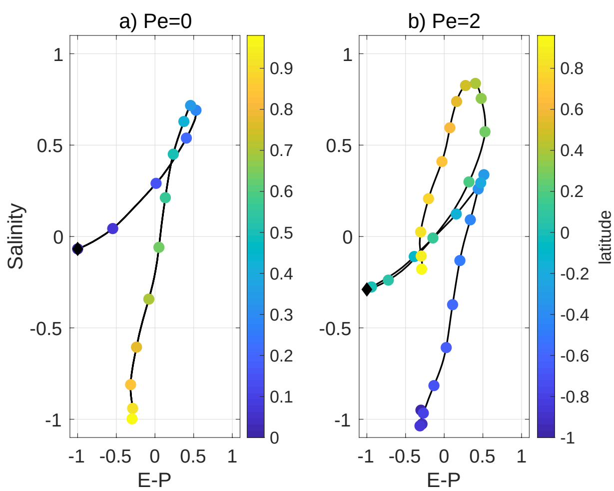


FIG. 7. Relations between evaporation and salinity for the solutions shown in Fig. 6a, with an equatorially-symmetric net evaporation field that resembles the Atlantic one. A purely diffusive solution, which is equatorially symmetric (panel a, Pe = 0), and an advective-diffusive solution (panel b, Pe = 2) are shown. The color indicates the latitude ($y/L$) and the black diamond marks the equator. Note that panel a) shows only the northern hemisphere ($0 < y/L < 1$), whereas panel b) shows both hemispheres ($-1 < y/L < 1$).

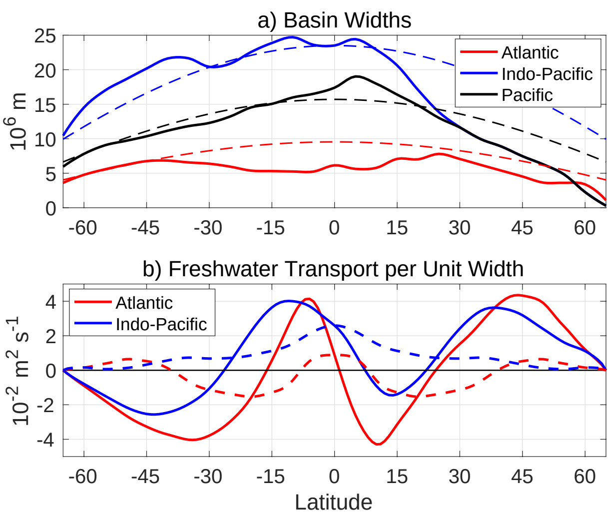


FIG. 8. a) Zonal widths of the Atlantic, Indo–Pacific and Pacific basin sectors obtained using the basin masks of Zweng et al. (2013). The dashed lines show widths of basin sectors with a constant longitudinal extent. b) Freshwater transports per unit width $G(y)$ [see Eq. (19)] for the Atlantic and Indo–Pacific basin sectors, calculated from the ERA-Interim reanalysis for 1979–2012 (Dee et al. 2011) as described in the text. Dashed lines show the equatorially symmetric parts of $G(y)$, which is tied to the equatorial asymmetry of the net evaporation fields. Note that the meridional freshwater transport [$F = B \cdot G$, see Eq. (18)] is greater in the wider Indo–Pacific sector than in the Atlantic sector.

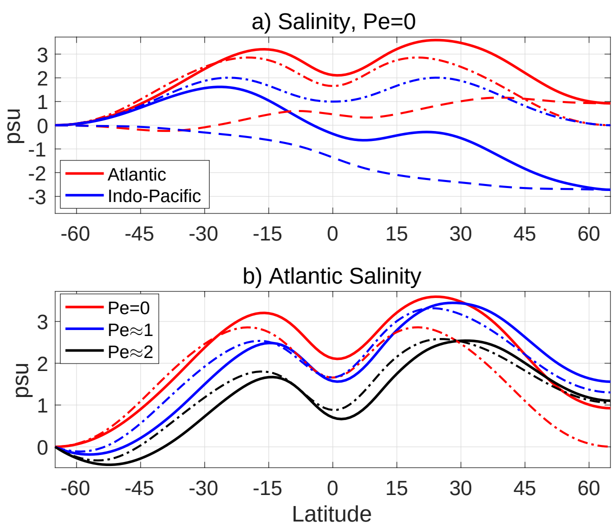


Fig. 9. a) Diffusive salinity solutions (Pe = 0) calculated from Eq. (20) using the data shown in Fig. 8. The dashed/dashed-dotted lines show the salinity field obtained by using the equatorially-symmetric/equatorially-antisymmetric parts of the freshwater transport $G(y)$. b) Atlantic advective-diffusive salinity fields calculated using the same data as in a); see the text and the appendix for details. Dashed-dotted lines show the salinity field obtained by using the equatorially-antisymmetric parts of $G(y)$. (The red lines duplicate the Atlantic diffusive Pe = 0 solutions in panel a). Note that as the Atlantic basin width vary slightly, the Peclet numbers vary with latitude, but these variations are modest; see Eq. (21). In both panels the parameter $\kappa h$, which controls the amplitude of the salinity variation, is $1.5 \cdot 10^6$ m$^3$ s$^{-1}$.

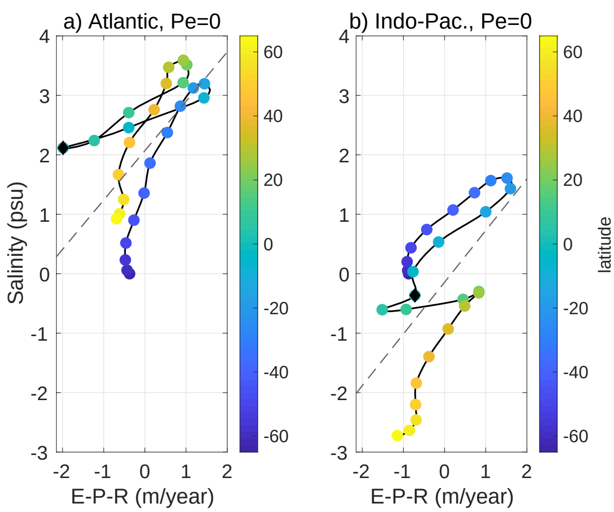


FIG. 10. Atlantic (a) and Indo–Pacific (b) relations between net evaporation and salinity from the diffusive solutions (Pe = 0) defined by Eq. (20); shown in Fig. 9a. The dashed lines show straight line least square fits to the data (Eq. 2): the slope in the Atlantic (Indo–Pacific) corresponds to a salinity change of 0.8 (1.2) psu per m year$^{-1}$.

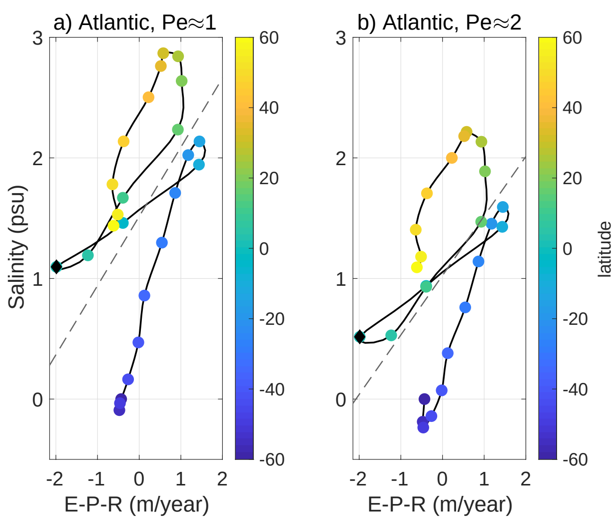


FIG. 11. Atlantic relations between net evaporation and salinity from the advective- diffusive salinity solutions with (a) Pe $\approx$ 1 and (b) Pe $\approx$ 2, shown in Fig. 9b. The dashed lines show straight line least square fits to the data (Eq. 2): the slope in panel a (b) corresponds to a salinity change of 0.6 (0.5) psu per m year$^{-1}$.

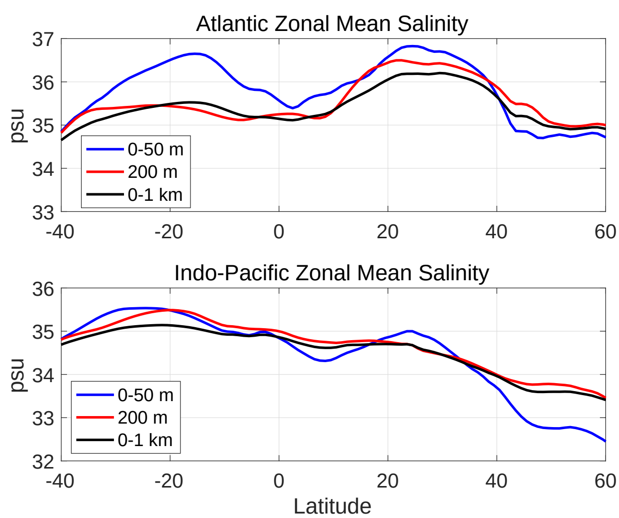


FIG. 12. Zonal-mean salinity in the Atlantic (a) and Indo–Pacific (b). The blue (black) line shows the salinity vertically averaged from the surface down to 50 (1000) m, and the red lines show the salinity in the thermocline at 200 m. Data is from the World Ocean Atlas 2013 (Zweng et al. 2013).

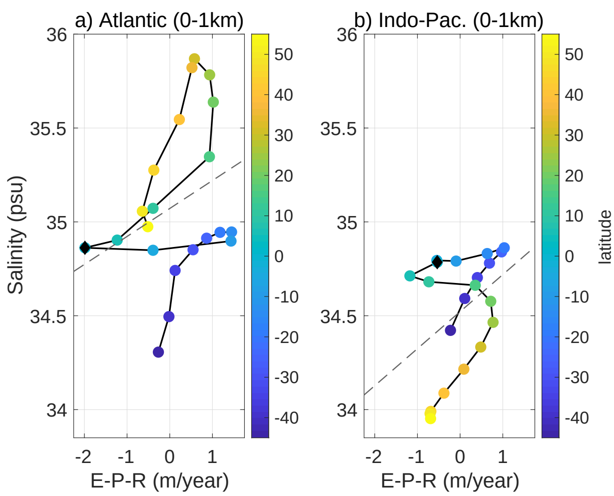


FIG. 13. A diagram with zonal-mean net evaporation (adjusted for river runoff) on the $x$ axis and the zonal-mean salinity averaged over the upper 1000 m on the $y$ axis. Climatological salinity from Zweng et al. (2013) is used. Panel a/b shows the Atlantic/Indo–Pacific Basins from 40°S to 55°N; the northern limit is chosen to exclude parts in the North Pacific where large areas are shallower than 1000 m. The colour scale indicates the latitude and the black marker shows the equator. Dashed lines show regression least square fits (Eq. 2) to the data. The slope in the Atlantic (Indo–Pacific) corresponds to a salinity change of 0.17 (0.25) psu per m year$^{-1}$. When the data is area-averaged in subpolar and subtropical latitude bands, the Atlantic $\tilde{E}$–$S$ relation (not shown) becomes qualitatively similar to the Pe = 2 model solution shown in Fig. 6b.